DESIGN AND MICROFABRICATION OF A STRAIN-GAUGE ARRAY ON POLYMER SUBSTRATE FOR TACTILE NEUROPROSTHESIS IN RATS

by

Mohammad Beygi

B.S., Electrical and Electronics Engineering, Urmia University, 2013

Submitted to the Institute for Graduate Studies in
Science and Engineering in partial fulfillment of
the requirements for the degree of
Master of Science

Graduate Program in Electrical and Electronics Engineering Department

Boğaziçi University

2016

to my brother, Amir

for his endless support, encouragement and irreplaceable advices

ACKNOWLEDGEMENTS

First, I would like to express my greatest appreciation to my advisor and co-advisor Dr. Senol Mutlu and Dr. Burak Güçlü for their never-ending support and advices, without whom I could never think of succeeding in my research. Their encouragement and advices have been always a big leading. Thank you for your patience, for your kindness and all the invaluable knowledge that I learned from you during this time.

Next, I would like to express my deepest gratitude to my parents for dedicating all their life and soul to support me. I am very grateful to have such kind parents. Thanks to all my family, particularly my wonderful brother, Amir, whose help and support was always a great blessing, who is always my best friend and best paragon.

Additionally, I express my warmest thanks to my best friends, who have helped me during these years, accompanied me during my difficulties and happiness; to Manouchehr Nadjafi, Gholamreza Ilkhani, Sina parsnejad, Mehdi Madani, Hossein Mazaheri, Mohammad Ali Vosoughi, Shahrzad Zahertar, Aida Sadeghzadeh, Ata Sarrafinezhad, Mohammad aziziaghdam and other friends with whom we were a big family.

And last but not least, I would like to thank BUMEMS and TACLAB members for their help and kindness. Particularly, thanks to Ismail Devecioğlu and Ozan Ertop for their help and advices during fabrication and experiments.

Some sections of this work have been presented in Micromechanics and Microsystems Europe Conference (MME) in Toledo, Spain; and published in Journal of Micromechanics and Microengineering (JMM).

This study is supported by TÜBİTAK with grant no: 113S901 and Boğaziçi University BAP no: 15XD2 given to Dr. Burak Güçlü.

ABSTRACT

DESIGN AND MICROFABRICATION OF A STRAIN-GAUGE ARRAY ON POLYMER SUBSTRATE FOR TACTILE NEUROPROSTHESIS IN RATS

In this work design, microfabrication and characterization of a strain gauge array which can be used for sensory neuroprostheses in rats is presented. The array is composed of an array of 2×7 cells, each of which has a series combination of 4 strain gauges. Each group of four strain gauges is placed around a square membrane with the size of 2.5×2.5 mm^2. Unlike most common tactile sensors based on silicon substrate, we used 3D-printed polylactic acid (PLA) as a substrate. Strain gauges were fabricated by depositing and patterning a thin aluminum (Al) film on a polyimide sheet with a thickness of 0.125 mm. Polydimethylsiloxane (PDMS) elastomer was bonded on the top surface of the polyimide membrane. PDMS layer is prepared in two different thicknesses for the sake of a comparative investigation into influence of the thickness of the elastomer membrane in static response of the sensor. The maximum allowable force corresponding to a maximum deformation of 0.9 mm of the center of each cell in two sensors differs according to the thickness of PDMS layer. The average force that each sensor cell operates linearly is 3N with an average resistance variation of 200 mΩ/N (for the sensor with 1.2-mm thick PDMS) and 4 N with an average resistance variation between 70 mΩ/N (for the sensor with 1.5-mm thick PDMS), and a nonlinearity of less than 3%. The cells have comparatively low average cross-talk around 5 mΩ/N. The static response of the cells was calibrated by using a micromanipulator and a digital balance and dynamic response of the individual cells of the sensor was characterized at several frequencies by using a vibrotactile stimulation system and a high gain amplifier. Then the sensor was tested inside the conditioning chamber to demonstrate the reliability of the sensor response for both static and dynamic stimulations.

ÖZET

SIÇANLARDA DOKUNSAL NÖROPROTEZ UYGULAMASI İÇİN POLİMER TABANLI GERİNİM-ÖLÇER DİZİSİ TASARIMI VE MİKROFABRİKASYONU

Bu çalışmada sıçanlarda dokunma duyusu nöroprotezi için kullanılabilecek bir sensör sisteminin tasarımı, mikrofabrikasyonunu ve testleri yer almaktadır. Sensör sistemi her hücrede dört adet seri bağlı gerinim-ölçer bulunan 2×7 hücreli bir diziden oluşmaktadır. Tüm dörtlü gerinim-ölçer grupları, 2.5×2.5 mm^2 boyutlarındaki kare membranın etrafına yerleştirilmiştir. En yaygın olarak kullanılan silisyum tabanlı dokunsal sensörlerin aksine, taban olarak üç boyutlu yazdırılmış polilaktik asit (PLA) kullanılmıştır. PLA kırılgan olmadığı için ve bölgesel hasarları tolere ederek bütün sensörün bozulmasını engellediği için uygun bulunmuştur. Gerinin-ölçerler, 0.125 mm kalınlığındaki poliimid filmin üzerine 50 nm kalınlığında alüminyum (Al) filmin kaplanması ve şekillendirilmesi ile üretilmiştir. PI membranın üzerine polidimetilsiloksan (PDMS) elastomer yapıştırılmıştır. Sensörün statik yüklemelere cevabını incelemek için, PDMS katmanı 1.2 mm ve 1.7 mm olarak iki farklı kalınlıkta hazırlanmıştır. PDMS katmanının kalınlığına bağlı olarak duyarlılık ve hücrelerin merkezinde maksimum 0.9 mm deformasyona karşılık gelen en yüksek kabul edilebilir kuvvet beklendiği gibi değişmektedir. 1.2 mm kalınlığındaki PDMS için, sensör hücreleri 200 mΩ/N (0.7 Ω/mm) ortalama duyarlılıkla, 3 N'a kadar doğrusal olarak çalışmıştır. Bu değerler 1.7 mm kalınlığındaki PDMS için, 70 mΩ/N (0.3 Ω/mm) ve 4 N olarak bulunmuştur. Doğrusallıktan sapma %3'ten daha az ölçülmüştür. Hücrelerin arasındaki etkileşim ortalama duyarlılıkla karşılaştırıldığında düşüktür (~ 5 mΩ/N ve 0.02 Ω/mm). Ayrıca sensörün dinamik cevabı daha önce psikofizik deneyleri için tasarlanmış bir titreşimsel mekanik stimülasyon sistemi kullanılarak değişik frekanslarda ölçülmüştür. Son olarak dokunma duyusu nöroprotezlerinde kullanılan işaret işleme yöntemlerini göstermek amacıyla sensör sistemi sıçan şartlandırma kabininde de test edilmiştir.

TABLE OF CONTENTS

ACKNOWLEDGEMENTS iv
ABSTRACT v
ÖZET vi
TABLE OF CONTENTS vii
TABLE OF FIGURES ix
LIST OF TABLES xi
LIST OF SYMBOLS xii
LIST OF ACRONYMS/ABBREVIATIONS xiii
1. INTRODUCTION 1
2. THEORY AND CONCEPTS 6
2.1. Stress and Strain Analysis 6
2.1.1. Stress 6
2.1.2. Strain 7
2.1.3. Plane Stress 10
2.1.4. Plane Strain 10
2.1.5. Yield Stress 10
2.1.6. Plastic Deformation 11
2.1.7. Bending of Plates 12
2.1.8. Square Membranes 13
2.2. Dynamic Analysis 15
2.2.1. Single Degree of Freedom Spring-Mass-Damper (SMD) System 15
2.2.2. Resonance Frequency 17
2.3. Resistivity and Gauge Factor 17
2.4. Chemistry of Materials 19
2.4.1. PDMS 19
2.4.2. Polysiloxanes 20
2.4.3. Polyimide 23

2.4.4. Plasma Surface Treatment 24
2.4.5. Aluminum Deposition and Thermal Evaporation 26
2.4.6. Etching 28
2.4.7. Aluminum Etching 29
3. DESIGN AND SIMULATION 31
3.1. Comparison of Mathematical Calculation and Simulation Results 31
3.2. Dynamic Simulation of Sensor 35
4. FABRICATION 39
4.1. Strain gauge patterning 39
4.2. PDMS and substrate preparation 41
4.3. Sensor integration 42
5. CHARACTERIZATION AND TEST 44
5.1. Static Characterization 44
5.2. Dynamic Characterization 48
5.3. Sensor Test 50
6. DISCUSSION AND CONCLUSION 54
7. FUTURE WORK 57
REFERENCES 61
APPENDIX A: SENSOR MASK 69
APPENDIX B: SAMPLES OF RECORDED RESULTS 70
B.1. Samples of Static Results 70
B.2. A Sample of Dynamic Results 74

TABLE OF FIGURES

Figure 1.1. Operation of a tactile neuroprosthesis for the rats... 2

Figure 1.2. Intended design of the sensor. 5

Figure 2.1. Stress tensors on a partition separated from a structure. 7

Figure 2.2. Proportionality between strains in different directions. 9

Figure 2.3. Behaviors of two brittle and ductile materials. 11

Figure 2.4. Single degree of freedom SMD system inside. 16

Figure 2.5. Representative formulas of various types of chains in polymers. 20

Figure 2.6. Bonding of elements in a siloxane unit. 21

Figure 2.7. Chemical structure of polyimide.. 23

Figure 2.8. Illustration of a thermal evaporation system including main parts. 28

Figure 2.9. Difference between isotropic and anisotropic etchings............................... 29

Figure 3.1. Plane stress on the bottom surface of PI. 32

Figure 3.2. (a) COMSOL simulation results showing stress distribution....................... 34

Figure 3.3. (a) The cross-sectional view of a cell and the direction of applied force..... 36

Figure 3.4. Results of dynamic simulation of the membrane in COMSOL. 37

Figure 4.1. Cross-sectional view of the sensor system. 39

Figure 4.2. Steps in fabrication of Al strain gauges on PI sheet. 40

Figure 4.3. PDMS sheet peeled off from the plastic container. 41

Figure 4.4. (a) Fabricated sensor array. 43

Figure 5.1. (a) The system used for static characterization of the fabricated sensor. 45

Figure 5.2. Static characterization results of the fabricated sensors. 46

Figure 5.3. Cross-talk measurements. 47

Figure 5.4. Effects of probe distance on resistance change. 48

Figure 5.5. Tactile psychophysics setup. 49

Figure 5.6. Dynamic characterization results of one sensing element. 50

Figure 5.7. Side view of the operant chamber. 51

Figure 5.8. Results from the rat operant chamber. 52

Figure 7.1. The interface which can be used for preparation the sensor signals 58

Figure A.1. Lithography mask. 69

Figure B.1. Voltage variation results obtained by DC characterization system. 73

Figure B.2. Dynamic signal recorded from sensor. 74

LIST OF TABLES

Table 3.1. Values for calculating stress on a membrane. 32

Table 3.2. Properties of the materials used for simulation purpose. 35

Table 3.3. Spring constant and resonance frequency of the membrane. 38

LIST OF SYMBOLS

D	Flexural rigidity
E	Young's modulus
G	Shearing modulus
P_m	Plate modulus
ω_n	Natural frequency
ω_r	Resonance frequency
ν	Poisson's ratio
ρ	Density
σ	Stress

LIST OF ACRONYMS/ABBREVIATIONS

Al	Aluminum
DI	Deionized
EMI	Electromagnetic interference
ICMS	Intracortical microstimulation
IPA	Isopropyl alcohol
PDMS	Polydimethylsiloxane
PI	Polyimide
PLA	Polylactic acid

1. INTRODUCTION

Tactile perception is essential for exploring the environment, manipulating objects, and socializing in humans and animals. For this reason, adding tactile feedback to neuroprostheses would be a significant milestone for individuals who could benefit from these devices [1-3]. In such a system, the mechanical tactile information obtained by artificial sensors on the neuroprosthesis is converted to signals mimicking neural impulses, and these are sent through implanted electrodes which electrically stimulate a specific area in the somatosensory cortex [4,5] or through intrafascicular electrodes for stimulating peripheral nerves [6,7]. All information from various receptors in different parts of the body are conveyed through the neurons and somatosensory region of the cortex has neurons from these various regions. When some connections of these neurons are lost due to some traumas, electrical pulses can stimulate a specific area of the somatosensory cortex instead, and as the result the same sense in the body part connected to that region may be elicited. This technique is commonly called intracortical microstimulation (ICMS) and has been used in behavioral experiments mostly with monkeys. Generally, tactile neuroprosthesis prototypes based on ICMS are tested in detection and intensity/frequency discrimination experiments. For example, in [4], the mechanical stimulation was detected by the strain gauges in the Modular Prosthetic Limb developed by Johns Hopkins Applied Physics Laboratory. The voltage signal obtained from a standard Wheatstone configuration was digitized and converted to ICMS pulse trains with varying electrical current amplitudes. The monkeys could perform the detection task with mechanical vibrations of different displacement amplitudes applied on the robotic finger. However, the robotic finger was stationary; in other words, it acted as a passive sensor for the animal.

The main goal in neuroprostheses is combining the movement of body parts to the proprioceptive and tactile sensation and the main goal of this work is emulation of neuroprostheses in rats. To make sure that using this approach the results are so reliable, traumas should be lowered in animals. So, for avoiding amputation, a boot is required which isolates the receptors of the feet from the stimulation, and instead a sensor is attached on it to detect the mechanical stimulation in a vibrotactile stimulation system [8].

The operation of the tactile neuroprostheses system is depicted in figure 1. First, using this system a mechanical stimulation is generated. Using a manual program in a computer the signals which are used for driving a mechanical shaker in the system are generated (A). These electric signals drive the shaker after amplification using a power amplifier and filtering (B). Then the shaker stimulates the sensor bonded to the rats' boot (C). And then the signals generating in the sensor, are sent back to the computer after filtering and amplification (E). The computer also controls different functions in the chamber (H). The signals received from the sensor system to the computer are delivered to the ICMS system to generate ICMS pulses in real time (F). Based on some models the ICMS system generates current pulses and these pulses are conveyed to the somatosensory cortex (G). The closed-loop operation shown in figure 1 facilitate the embodiment of the tactile neuroprosthesis as the animal moves with it [65]. Here, we present the design, microfabrication technique, and the characterization results of the tactile sensor array to be placed under the hind-paw boot.

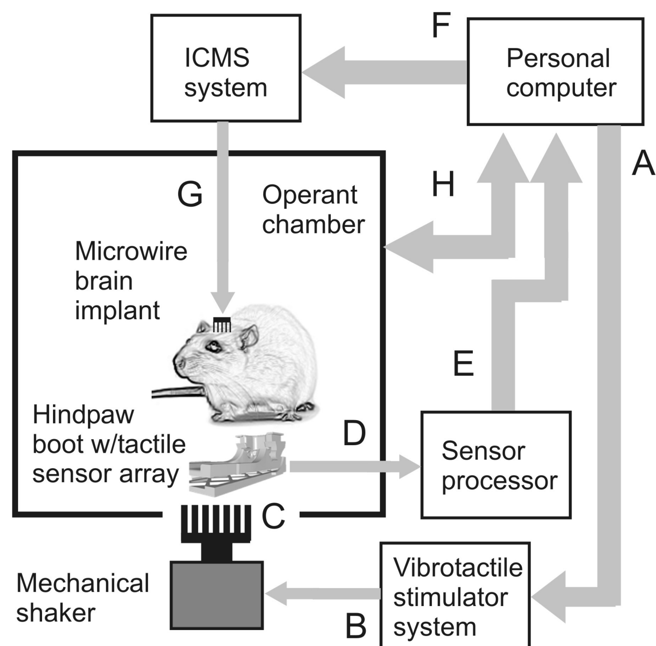

Figure 1.1. Operation of a tactile neuroprosthesis for the rats. The signals are labeled in capital letters and explained in text [65].

Tactile sensors detect surface texture of objects and distribution of contact forces [9]. Several different approaches exist in the literature for tactile sensing. These include capacitive sensors [10,11], piezoresistive [12,13], piezoelectric [14,15], and metallic strain

gauges [16,17]. Many of these sensors use silicon as the fundamental material for the substrate. Due to the brittle nature of silicon, it is difficult to handle large deformations and measure high forces with silicon-based sensors for neuroprosthetics applications [18]. In our specific application, the animal moves freely during inter-trial periods of a behavioral experiment and generates unpredictable forces on the sensor. Due to its brittleness, a silicon substrate may break and result in catastrophic failure of all cells in the array. Because of the complex micromachining method of silicon, the final product is also more expensive. Linearity, bandwidth, the maximum displacement that the sensor tolerates, low cross-talk between the cells, simplicity of the fabrication technique, and higher flexibility are among the major challenges of tactile sensors. For example, in [10,11], capacitive sensors with metallic electrodes and polydimethylsiloxane (PDMS) layers were presented. These capacitive sensors have good sensitivity and large dynamic range. However, cross-talk and complexity of the required electronic circuitry are important drawbacks. In [12], a piezoresistive tactile sensor which had a boron-doped silicon sensing element was reported. High sensitivity (3.36% relative resistance change per Newton), flexibility and simple electronics were among the advantages of this sensor. However, the fabrication was still complex, and the highest displacement and force limits were lower than those expected for our neuroprosthetics application. A different piezoresistive sensor was introduced in [13]. This sensor had a silicon piece sandwiched between two flexible PDMS layers. The sensor had a high sensitivity of 0.122 mV/V/kPa, high flexibility and good linearity, but could not detect pressure values below 80 kPa. Piezoelectric sensors were developed in [14,15]. These sensors generally have wide bandwidths and high sensitivity. However, they can only detect dynamic stimuli and generate AC outputs. Since they do not respond to static indentations, they are not suitable in our application. In [16,17], metallic strain gauges were placed in an array. Both studies, similar to the work presented here, used thin metal deposition on polyimide (PI) film. Metallic strain gages have moderate sensitivity, but they are relatively easier to fabricate and can be very flexible. On the other hand, these studies did not design diaphragms or membranes to magnify strain. Instead, bulk PDMS layers or ridges were used to increase the deformation of the strain gauges. Because they were surrounded by soft polymer layers, these sensors would have lower bandwidth, which is undesirable for tactile feedback.

One of the limitations of tactile sensors mentioned in the literature is their low deformation capability, which differentiate them from biological skin with higher deformation capability. For example, in [9], a NiCr metallic strain gauge was used as the sensing element. A layer of polyimide (PI) was formed as the membrane of the sensor and another layer of elastomer was used to coat the surface for protecting the lower layer. Although the fabrication technique is easy, the maximum force of the linear range (0-0.6 N) is not high enough for our application. In a different study [18], NiCr was deposited on a coated PI surface and etched to form strain gauges. The sensor surface worked on a silicon substrate. Although the sensitivity (0.61 Ω/μm) and the linearity were good, it had a maximum tolerable displacement of 15 μm limited by the membrane cavity.

The sensor which is appropriate for our neuroprostheses system should have some specifications which none of the approaches in literature mentioned above have altogether. The tactile sensor should be able to respond properly to both dynamic and static stimulations. It should tolerate large displacements as well as smaller displacements in the range of tens of micrometer. It should be stiff enough to handle higher amount of forces, so that silicons based sensors can not be a good choice due to its brittle nature. It should have multi-sensing elements, in case of damages to couples of them some elements still remain. Since the possibility that the sensor gets damaged during the experiments is so high, then the fabrication method should be inexpensive and simple.

Some of the specifications that we expect to see in our designed sensor are listed below.

- High sensitivity
- Maximum tolerable force of 3 N (based on the weight of the rats)
- Dynamic range of 40 dB
- Linear response by the deformation in the range of 0-900 μm
- Enough flexibility comparable with flexibility of rats' glabrous skin
- Easy, inexpensive, durable and robust fabrication method
- Low cross-talk, much lower than the sensitivity of the sensor
- Embeddable with the boot built of PLA
- Biodegradability

- With cell surface perimeter less than the probes' perimeter
- Protection against EMI
- With the same size as the boot designed for the rats
- Having multiple cells (numbers of cells are limited by fabrication technology)
- Independent sensor elements

To achieve the specifications mentioned above in our sensor, we adopted polylactic acid (PLA) as a substrate and produced it by a desktop 3D printer. PLA is biodegradable and does not break due to chewing or high forces applied by the animal. Our sensing elements are thin film aluminum (Al) strain gauges formed on the surface of a thin PI sheet. A layer of cured PDMS was also used to protect this PI film. The PDMS layer contacts the stimulus for tactile sensing. Since our mechanical shaker has moving probes for stimulation [8], we have a flat sensor surface instead of bumps or similar convexities. The hind-paw boot has a separate deflecting part which isolates the animal's skin from the vibrations applied by the shaker underneath. The tactile sensor is attached to this part and should be flexible enough to bend under pressure produced by the weight of the animal. Our design has acceptable sensitivity and low cross-talk. Size and shape of the sensor are shown in figure 1.2.

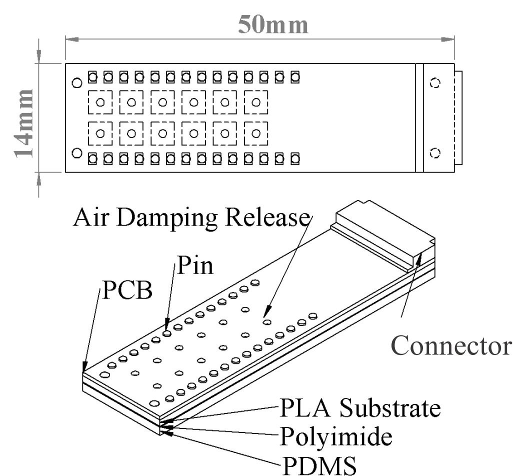

Figure 1.2. Intended design of the sensor.

2. THEORY AND CONCEPTS

2.1. Stress and Strain Analysis

In this section an explanation on elastic material and theory of elasticity for isotropic material will be presented. Indeed, elastic materials such as PDMS or PI that we used in our sensor, are among those material that may change their shape under a force, and when they become free from the force their shape will return to the initial state. In this part we assume that our material is completely isotropic, so that its physical properties are similar in the whole body, in all axes.

When talking about elasticity, perhaps what mostly come to one's mind are two important definitions; stress and strain. Our design and fabrication is also based on these two important definitions. Strain gauges' functionality is based on strain and its effect on resistance. So, in following section we will define these two terms and present different types of strain and stress that may exist in a structure under a force.

2.1.1. Stress

Stress is defined as the force applied to a small unit area of a continuum. Therefore, its unit is N/m^2 [19]. Actually, stress is produced by internal forces between the internal portions of a subject under an external force. Generally, stresses acting on a surface are divided into two categories, one is normal stress which are perpendicular to the surface (as the stimulator pins affects the surface of the sensor), and another is shear stress (when the angle of the stimulator pins is not right, then one element of the force is horizontal to the surface of the sensor) which is along the surface. If a very small element of a structure is separated from the whole, the stress distribution over each surface is as illustrated in figure 2.1.

The element is in static equilibrium, so that no torque or net force is induced. On each surface there are three stress vectors, one of which, perpendicular to the surface, is normal stress and the other two are shear stresses which are along the surface [19].

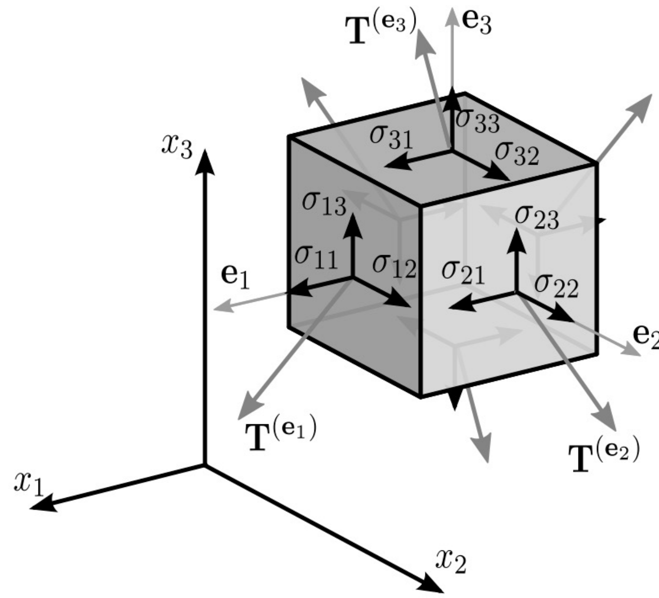

Figure 2.1. Stress tensors on a partition separated from a structure.

In figure 2.1. normal stresses are σ_{11}, σ_{22}, σ_{33} and shear stresses are σ_{12}, σ_{13}, σ_{21}, σ_{23}, σ_{31}, σ_{32}. The right side of this cubic shape also follows this rule. Considering the equilibrium condition, shear stresses may be summarized to σ_{12}, σ_{13}, σ_{23}, since in equilibrium $\sigma_{12} = \sigma_{21}$, $\sigma_{13} = \sigma_{31}$, $\sigma_{23} = \sigma_{32}$.

In sake of simplicity, as mentioned above stress tensors can be summarized as follow.

$$\sigma = \begin{bmatrix} \sigma_{11} & \sigma_{12} & \sigma_{13} \\ \sigma_{12} & \sigma_{22} & \sigma_{23} \\ \sigma_{13} & \sigma_{23} & \sigma_{33} \end{bmatrix} \quad (2.1)$$

2.1.2. Strain

When stress is applied to a material, it will be deformed. The changes in the size of a structure per unit length is called strain (the phenomenon that happens in strain gauges). For one dimensional material as shown in figure 2.2, if the original position is shown using u(x) and the displaced position, u(x+Δx), then one dimensional displacement is as follow [21],

$$\epsilon_x = \lim_{\Delta x \to 0} \frac{u(x + \Delta x) - u(x)}{\Delta x} \cong \frac{\Delta u_x}{\Delta x} = \frac{\partial u}{\partial x} \tag{2.2}$$

As previously explained, due to shear stress, shear strain is also induced in the material. For shear strain, accordingly, we have:

$$\epsilon_{xy} = \left(\frac{\Delta u_x}{\Delta y} + \frac{\Delta u_y}{\Delta x}\right) = \left(\frac{\partial u_x}{\partial y} + \frac{\partial u_y}{\partial x}\right) \tag{2.3}$$

Using above approach for three-dimensional structures, below matrix is obtained which includes both normal and shear strains:

$$\begin{bmatrix} \Delta u_x \\ \Delta u_y \\ \Delta u_z \end{bmatrix} = \begin{bmatrix} \frac{\partial u_x}{\partial x} & \frac{\partial u_x}{\partial y} & \frac{\partial u_x}{\partial z} \\ \frac{\partial u_y}{\partial x} & \frac{\partial u_y}{\partial y} & \frac{\partial u_y}{\partial z} \\ \frac{\partial u_z}{\partial x} & \frac{\partial u_z}{\partial y} & \frac{\partial u_z}{\partial xz} \end{bmatrix} \begin{bmatrix} \Delta x \\ \Delta y \\ \Delta z \end{bmatrix} \tag{2.4}$$

The proportionality between stress and strain is explained by *Hook's law*. For isotropic material, there's a linear relation between stress appeared in the material and its deformation. Based on this law, with using Young's Modulus, one can define how much change on the dimensions of an isotropic material emerges if that material is under stress [19]. Thus, a normal stress in any direction can cause a uniaxial strain on that direction:

$$\sigma = E\epsilon \tag{2.5}$$

Since strain is unitless, so that Young's Modulus unit is N/m^2. So, the unit of E is the same as stress unit.

If a free-standing material is under a normal stress in one specific axis, this stress can cause changes on dimensions of the material in the other axes. For example, in figure 2.2 there's a normal stress in x-axis. Since the material is free, this stress not only gives rise to the extension of the material in x direction, but the material also shrinks in y-direction. Thus, in one direction it makes positive strain while in other direction the strain is negative.

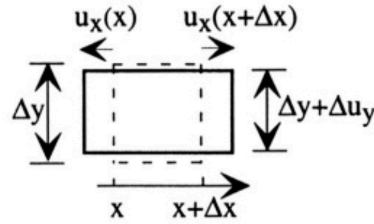

Figure 2.2. Proportionality between strains in different directions [20].

This proportionality between the strains in different directions can be defined using the constant Poisson's ratio, ν. For linear isotropic material the equation shown below is used to define this relation:

$$\epsilon_y = -\nu\epsilon_x \tag{2.6}$$

Similar to strain, Poisson's ratio is unitless and also dimensionless. This ratio is usually considered between 0 and 0.5. However, some materials with a negative Poisson's ratio have also been found.

If considering a condition in which a structure is under a stress, it's experimentally been proven that in order to find the value of the total strain, stresses in all directions should be taken into consideration. Therefore, a more comprehensive equation is brought below.

$$\epsilon_x = \frac{1}{E}\left(\sigma_x - \nu\left(\sigma_y + \sigma_z\right)\right) \quad (2.7)$$

$$\epsilon_y = \frac{1}{E}\left(\sigma_y - \nu(\sigma_x + \sigma_z)\right) \quad (2.7)$$

$$\epsilon_z = \frac{1}{E}\left(\sigma_z - \nu\left(\sigma_x + \sigma_y\right)\right) \quad (2.7)$$

As observed, similar to normal strain there's a relation between shear stress and shear strain which is defined as below:

$$\sigma_{xy} = G\epsilon_{xy} \tag{2.8}$$

In which G is shearing modulus constant defined as follow:

$$G = \frac{E}{2(1+\nu)} \tag{2.9}$$

2.1.3. Plane Stress

If the boundaries of a thin plate or membrane, whose thickness comparing to its length is very small, is exposed to a normal force and this force results in a distributed stress inside the material in all directions, the stress within the thickness shall be neglected and just stresses along the peripheries shall be considered [20] (the stress that may impact the surface of the sensor). In this case stress components σ_z, σ_{zy}, σ_{zx} can be considered zero, so that the components σ_x, σ_y, σ_{xy} are the only ones should be taken into account.

2.1.4. Plane Strain

The similar definition can be used for strain but in a structure with a very large dimension in z-direction. When, for example, a cylindrical shape is under a uniformly distributed force perpendicular to the longitudinal elements, so it can be assumed that all cross sections have the same conditions and then there's no changes along the z-direction.

2.1.5. Yield Stress

We can categorize the material into two divisions based on how the structure behaves when under intensive stresses. The first group is brittle materials, in which stress-strain graph acts linearly up to a point called brittle fracture. When the strain passes this point, the material is broken. The second category is ductile materials whose stress-strain graph behaves linearly up to its yield point. When it crosses this point, by increasing strain, the stress appeared in the material remains constant until it meets the hardening region (such as PI that we used as the membrane of the sensor). Within this region stress increases until the

material breaks down. In the graph shown in figure 2.3 the behavior of these two distinct materials is shown [20].

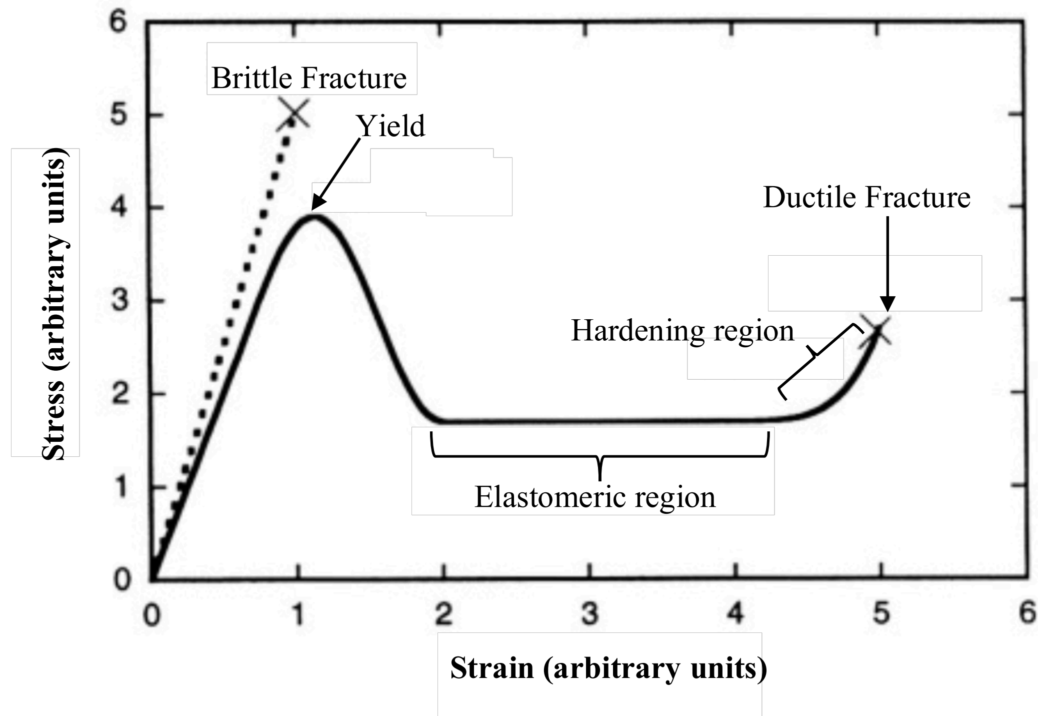

Figure 2.3. Behaviors of two brittle and ductile materials when strain increases gradually [20].

2.1.6. Plastic Deformation

According to plasticity, materials behave differently while they are under a force, and experience stress. When the plastic materials, for example metals, experience a force they may become deformed and temporarily lose their shape. When the force is released, the stress which previously occurs inside these materials, starts vanishing. When the stress completely disappears, still a residual strain remains on them which needs a negative stress to set it zero [20] (this phenomenon may happen in PI when the force is much enough to bring it to the plasticity region).

In contrast to metals, elastomeric materials don't experience this residual stress when they are under a certain amount of stress. In fact, when the force is released, they return to their former shape before experiencing the force.

There is another type of material based on this fact, called viscoelastic materials. Viscoelastic materials also behave similarly to a force, but in short time. Actually, the behavior depends strictly on the time that force remains. If the force continues to exist for a longer time, the material does not return to the former shape, which means it experiences residual strain. But if it takes shorter, so that the material becomes unloaded, then it won't have any residual strain (PDMS may experience this type of deformation state).

And the last category is related to thin film deposition. In this case, when the force is released from the substrate, since the deposited thin film has experienced a large amount of stress, it may behave differently comparing to the substrate. While the substrate has come back to the former shape, thin film may experience viscoelastic or plastic deformation. This is the condition that many thin film deposited structures may experience when they become bent (thin Al deposited on PI may experience this category when exposed to an intensive force).

2.1.7. Bending of Plates

In calculating bending of plates, first we assume that the plate is wide enough to estimate the equations with elimination of transverse Poisson contraction. Indeed, this approximation is just possible for rectangular plates in which one of the edges is much larger than another one. Actually for square plates the mathematics is very complicated, which will be mentioned at the end of this section. However, the only accurate way to solve equations for square membranes is using numerical methods such as finite element or finite differential method [20].

First, we shall start with assumptions mentioned above and then we expand the calculations to find the equations for square membranes. There are two important assumptions; first, the thickness of the plate is much lower than the sides of the plate, and second its dimension in one axis is larger than the other. With taking these two assumptions into account we have following equations:

$$\epsilon_y = 0 \tag{2.10}$$

$$\epsilon_x = \frac{1}{E}\left(\sigma_x - \nu\sigma_y\right) \tag{2.11}$$

And according to equation 2.10,

$$\epsilon_y = 0 = \frac{1}{E}\left(\sigma_y - \nu\sigma_x\right) \tag{2.12}$$

With combining the equations together, we have:

$$\sigma_x = \mathrm{P}_m\epsilon_x \tag{2.13}$$

$$P_m = \left(\frac{E}{1-\nu^2}\right) \tag{2.13}$$

The constant P_m is called plate modulus and its value is 10% larger than Young's modulus.

2.1.8. Square Membranes

Displacement calculation in square membranes is much harder than the equations for cantilever beams or rectangular plates. Numerical analysis is usually used for finding these values. In addition, there are some approximate mathematical methods which are used for this purpose. In these methods, as their names indicate, many approximation methods have been used with some constants which are experimentally obtained.

Using the energy method, an equation indicating the relationship between pressure and displacement is achieved. Length of the square is 2a, its thickness is t, and it is clamped in edges [21].

$$\omega(x,y) = \frac{1}{47}\mathrm{q}\frac{a^4}{D}\left(1-\frac{x^2}{a^2}\right)^2\left(1-\frac{y^2}{a^2}\right)^2 \tag{2.14a}$$

In above equation D is flexural rigidity which is defined by equation below.

$$D = \frac{1}{12} P_m t^3$$

And at the center of the membrane, maximum displacement is defined using the equation 2.14b.

$$\omega_{max} = \frac{qa^4}{64D} \quad (2.14b)$$

Using the equation 2.14 and the relation between the stress and the displacement on the surface of the membrane, stress equations on the surface are obtained as follow.

$$\sigma_x = -\frac{Ez}{1-\nu^2}\left(\frac{d^2\omega}{dx^2} + \nu\frac{d^2\omega}{dy^2}\right) \quad (2.15)$$

$$= -0.51\, \mathrm{q}\frac{a^2}{t^2}\left[\left(1-\left(\frac{y}{a}\right)^2\right)^2\left(1-3\left(\frac{x}{a}\right)^2\right) + \nu\left(1-\left(\frac{x}{a}\right)^2\right)^2\left(1-3\left(\frac{y}{a}\right)^2\right)\right]$$

$$\sigma_y = -\frac{Ez}{1-\nu^2}\left(\frac{d^2\omega}{dy^2} + \nu\frac{d^2\omega}{dx^2}\right) \quad (2.16)$$

$$= -0.51\, \mathrm{q}\frac{a^2}{t^2}\left[\left(1-\left(\frac{x}{a}\right)^2\right)^2\left(1-3\left(\frac{y}{a}\right)^2\right) + \nu\left(1-\left(\frac{y}{a}\right)^2\right)^2\left(1-3\left(\frac{x}{a}\right)^2\right)\right]$$

Using equations 2.15 and 2.16, the maximum stresses which appears in the middle of each edges can be calculated. The value of these stresses are presented in 2.41 and 2.42.

$$\sigma_x = 1.02\, \mathrm{q}\frac{a^2}{t^2} \quad (2.17)$$

$$\sigma_y = \nu\sigma_x \quad (2.18)$$

2.2. Dynamic Analysis

In addition to static response, the sensor that we designed is supposed to generate signals when exposed to to a dynamic stimulation. So, in this section we present the principles which we used to analyze dynamic response of our system.

In order to model dynamic system to acquire its frequency response, we shall use one degree of freedom system of spring-mass-damper. We can consider our elastic system as a chain of spring-mass-damper in order to calculate its resonance frequency. Obviously, if we exceed the number of this chain of structure we will acquire a more complex and more accurate equations.

In this chapter, we will describe one degree of freedom spring-mass-damper system, then we will derive the equations for this system, and finally we will use these equations in order to find its dynamic response. As a matter of fact, modeling our structure with one degree of freedom spring-mass-damper (SMD) system will not give us very accurate results, but using this approach we can build up a better understanding of dynamic of our system.

2.2.1. Single Degree of Freedom Spring-Mass-Damper (SMD) System

Consider figure 2.4 as a system of SMD, which are placed inside a movable frame. Let's consider the frame's moving downward as showing in the figure with y(t) and mass's moving in the same direction, x(t). So that, the overall movement from out-view is z(t), which is subtraction of y(t) from x(t).

The mass is pushed down by a static force, f_o, and also a time dependent force, $f(t)$. Moreover, another force called $F_r(z, \dot{z}, \ddot{z})$, which is caused by an external force like squeeze film damping, is defined. Due to the forces, an acceleration is occurred on the system while it's moving. In the right diagram in figure 2.4, different forces affecting the mass are shown. In this diagram F_s is the force applied by the spring; and F_d, the force applied by the damper.

Thus, the summation of the forces affecting the mass is as indicated in equation 2.19.

$$F_s + F_d + F_r(z, \dot{z}, \ddot{z}) + m\frac{d^2x}{dt^2} = mg + f_o + f(t) \qquad (2.19)$$

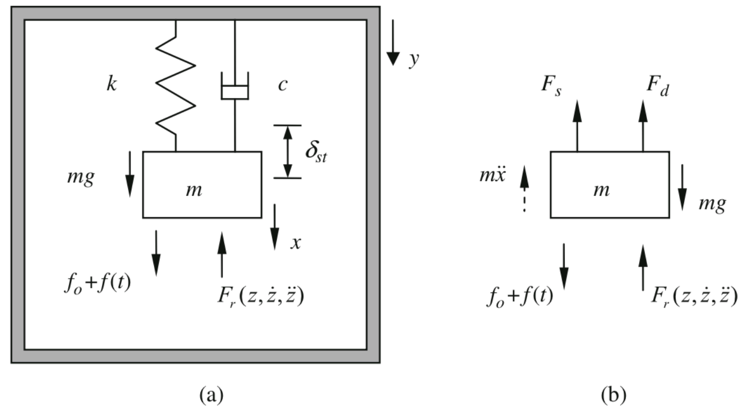

Figure 2.4. Single degree of freedom SMD system inside.

If saying the spring is extended as δ_{st}, and if we assume the spring behaves linearly with a spring constant of k, and the damper has a damping coefficient of c, then equation 2.20 is derived from equation 2.19.

$$k(z + \delta_{st}) + c\frac{dz}{dt} + \mathrm{F}_r(z, \dot{z}, \ddot{z}) + m\frac{d^2x}{dt^2} = mg + f_o + f(t) \qquad (2.20)$$

As mentioned earlier, the spring is linear and while static force effects it, it extends as δ_{st}. So, the value of δ_{st} can be obtained using equation 2.21.

$$\delta_{st} = \frac{1}{k}(mg + f_o) \qquad (2.21)$$

After substitution of this result to equation 2.20, for the static equilibrium condition 2.22 is obtained.

$$kz + c\frac{dz}{dt} + F_r(z, \dot{z}, \ddot{z}) + m\frac{d^2z}{dt^2} = f(t) - m\frac{d^2y}{dt^2} \qquad (2.22)$$

Considering a condition in which the frame's movement and the force caused by squeeze damping effect are zero, then equation 2.22 is more simplified and turned to be as equation 2.23.

$$kx + c\frac{dx}{dt} + m\frac{d^2x}{dt^2} = f(t) \tag{2.23}$$

In this case the natural frequency of the system is as follow [21].

$$\omega_n = 2\pi f_n = \sqrt{\frac{k}{m}} \left(\frac{rad}{s}\right) \tag{2.24}$$

2.2.2. Resonance Frequency

In the resonance frequency of a system, when a vibrating force is driving it, the amplitude of the vibration is the highest. If the natural frequency of the system is equals to ω_n, resonance frequency of the system is equal to $\omega_n\sqrt{1-2\zeta^2}$ for systems with very low damping effect. As the resonance frequency equation reflects, if the damping coefficient becomes very small and negligible, the resonance frequency of the system becomes similar to natural frequency of that system and the peak of the amplitude goes higher.

2.3. Resistivity and Gauge Factor

In order to define the gauge factor, which is a term to specify the sensitivity of different material to the strain that they are exposed to, first definition of resistivity is presented. Resistivity shows ability of material to oppose flowing of charge. The inverse of this property is called conductivity. There's a proportionality between electric field and current density of a material which is exposed to the electric field and resistivity of the material. As defined in [22], the resistivity has a direct proportionality with the electric field applied and a reverse proportionality with the current density of the material.

$$\rho = \frac{E}{J}\ (\Omega.m) \tag{2.25}$$

As mentioned earlier, this resistivity, in fact, is caused by the intrinsic properties of the material. Using physical properties and the geometry of the material, its resistance is calculated.

$$R = \rho \frac{L}{A}\ (\Omega) \tag{2.26}$$

Gauge factor defines the resistance changes in a specific material when it's under strain. Obviously, gauge factor is different among different materials, as this factor is dependent on their intrinsic properties [21].

In order to define and formulize gauge factor in metals (in our sensor aluminum), we consider a segment with the length of L and cross section of A. When this segment is under strain, a small amount of resistance change is observed in it. This small amount of resistance change is indicated with dR. According to resistivity's formula, this differential change in resistance is calculated as shown in 2.27.

$$dR = \frac{\rho}{A} dL + \frac{L}{A} d\rho - \frac{\rho L}{A^2} dA \tag{2.27}$$

And,

$$\frac{dR}{R} = \frac{dL}{L} + \frac{d\rho}{\rho} - \frac{dA}{A} \tag{2.28}$$

As explained in the previous section, strain is defined as follow.

$$\frac{dL}{L} = \epsilon \tag{2.29}$$

and also for cross section area, with width of W and height of H, the following equations are applied.

$$\frac{dA}{A} = \frac{dH}{H} + \frac{dW}{W} \tag{2.30}$$

$$\frac{dH}{H} = \frac{dW}{W} = -\epsilon\upsilon \tag{2.31}$$

in which υ is Poisson's ratio.
If substituting equations 2.27-31, equation 2.32 is derived.

$$\frac{dR}{R} = (1 + 2\upsilon)\epsilon + \frac{d\rho}{\rho} \tag{2.32}$$

The latter term, is negligible in metals. Then, metals' gauge factor is equal to:

$$GF = \frac{dR/R}{dL/_{L}} = (1 + 2\upsilon)\sim 2 \tag{2.33}$$

Although comparing to big gauge factor of diffused semiconductors the gauge factor of metals is very small, because of some other advantages which will be mentioned later, metallic strain gauges are still widely used for force and displacement measurement.

2.4. Chemistry of Materials

2.4.1. PDMS

As we used PDMS layer in our sensor, in this section we explain the properties of this material to make it clear why this material is suitable for our purpose.

According to [23], a polymer is a long chain of micromolecules in which hundreds or thousands of atoms are bonded together to form a larger one dimensional array. The skeletal atoms can be both small or large. These molecular structures are different from other molecules in the chains' capability to become entangled in solutions or in solid, and in some cases to be lined up in regular arrays in the solid state. Their molecular characteristics give

rise to some specific features that solid state materials own, such as their elasticity, strength, film-forming properties, etc.

Repeating units, which are a fairly simple structure repeating over and over down the chain, act exactly like the identification of polymers. Most synthetic polymers contain this identification with them, therefore distinguishing them is simply possible when noticing these repetitive chains. This polymer chains can be represented by either of formulas shown below.

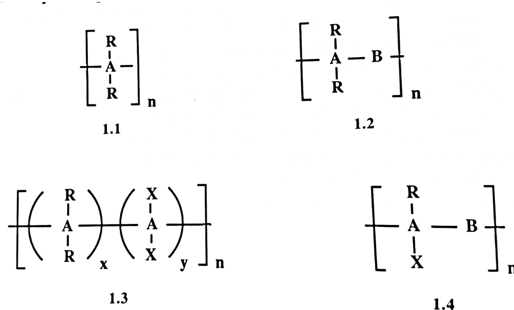

Figure 2.5. Representative formulas of various types of chains in polymers [23].

The exact number of these units are not specified in the formulas, but it's shown using subscript n. the skeletal groups in figure 2.5 are shown using different letters of X, R and B.

Polymers can be divided into two main groups of organic polymers and inorganic polymers. Most of the polymers in the nature are involved into organic polymers. This group of polymers mainly consist of carbon atoms separated by heteroatoms such Oxygen or Nitrogen. The other group of polymers have a chain of inorganic elements as well as organic elements on their structures. These inorganic elements give different features to polymers that otherwise would not be possible. Among all inorganic polymers, those which contain Silicon or Phosphorous in their macrostructure are more interesting.

2.4.2. Polysiloxanes

Polysiloxanes are types of polymer which has Si-O as the backbone of its polymer structure. Indeed, this bond gives the polymer very remarkable properties. For example, high strength of this bond causes a high thermal stability in this type of polymer, and thus makes it suitable for temperature applications. Moreover, the nature of the bonding and the

chemical characteristic of the side groups give the chain a very low surface energy and intriguing surface properties.

Another feature of this polymer which makes it different from other of the same type is huge difference between size of two Si and O atoms. This tremendous difference between their size gives the chain very irregular cross section. This, in fact, has influence in equation of state properties (such as compressibility). There are also other features which give it special properties such as bonding angels around the O atoms.

One of the most important properties of siloxane is its extraordinary flexibility that is much higher than all other polymers [24]. As indicated in figure 2.6, the unique bonding structure between the atoms can be the reason of this high flexibility [25,26,27]. The bonding between Si and O atoms are significantly larger than that of C-C. Generally, any single bond between inorganic atoms are larger than those of organic atoms. Due to this large distance, steric interfaces and molecular congestion are diminished. In addition, large angel bonding between Si-O-Si is also another reason, so that torsional rotations can occur with less energy expense [25].

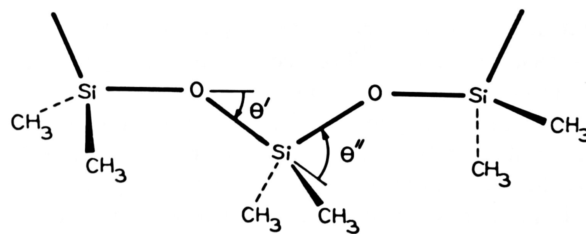

Figure 2.6. Bonding of elements in a siloxane unit [23].

Even with all these favorable properties, siloxane can not be used solely. So, in order to improve its properties, various additives should be used with siloxane. One of the typical approaches used mainly is a combination of siloxane and curing agents as reported in [28,29]. Depending on the specific cross-link chemical reaction of interest, different agents may be used. After mixing these curing agents with siloxane, curing process usually takes place in elevated temperature.

Poly dimethylsiloxane (PDMS), is an inorganic polymer which has siloxane backbone in its structure. PDMS is one of the common polymeric materials used for microfluidic devices because of its special features [30]. Monomer structure of this widely used polymer is [-$Si(CH_3)_2O$-]. Torsional barrier for rotation along its skeletal bonds is very low which makes this polymer highly flexible, with low temperature when transitioning from a hard state to a rubber-like state.

Another striking feature of siloxane polymers is their unusual surface properties. This unusual surface property permits them to serve seemingly different and contradictory roles. For example, siloxane polymers are both paper-release coating and pressure sensitive adhesive [31,32]. This unusual surface property is due to their low surface energies and surface tensions [31,32]. This is predictable because of very low inter-molecular forces between the side chains, which is methyl in PDMS, and the high flexibility of siloxane's back-bone which let the chain to change its arrangement in order for place the methyl in its interface or surface. For this reason, a surface damaged polysiloxane can quickly rearrange the surface characteristic of the original material.

Another feature of Polysiloxane materials is their tremendous durability and stability [33,34]. This property is caused by high oxidation state that the chains are in, and therefore they need high temperature for reduction of this state.

Furthermore, PDMS is a viscoelastic material. Physical properties of viscoelastic material change in different frequencies. Previously, this property of PDMS was neglected. With advancement in material science, it's now been proved that ignoring this feature results in errors in time and frequency dependent characterization of the applications [35,36].

Another fact which should be considered in application of PDMS is its surface preparation for bonding layers of other materials to PDMS. As previously mentioned, due to low surface energy of PDMS, forming tight bonding between surfaces would not be easy. So, in order to build a very tight bonding, a cross-link bond should be provided. To this aim, recently oxygen plasma has had a favorable result. Actually, the modification of the surface of the PDMS is occurred when it's exposed to the O_2 plasma. This exposure leads to a chain scission and oxidation of the surface [37]. Oxygen plasma can also result in formation of an

inorganic silica-like surface layer. This oxidation is, then, producing SiO_x, which is a silicon connected to three or four oxygen atoms [38].

To illustrate how this oxygen plasma treated PDMS is used for bonding, bonding of glass-PDMS surfaces is considered. Oxygen plasma treatment produces silica-like surface in PDMS which can form a permanent and leakage-free bond to the hydroxyl groups in the surface of the glass [39].

2.4.3. Polyimide

We used PI as the membrane of the sensor on which a layer of thin Al was deposited. Polyimide has long been used in the microelectronics industry as both insulator and packaging material. It is used in various forms including bulk (film or tapes) or spin-on versions [40] for both industrial and research purposes. Chemical structure of polyimide is shown in figure 2.7.

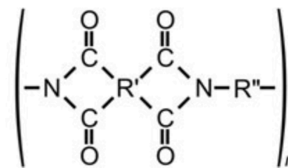

Figure 2.7. Chemical structure of polyimide. R' and R" can be either aliphatic or aromatic [23].

Widespread use of polyimide is significantly because of its low Young's modulus and also its bio-compatibility. Other notable properties of polyimide are its high thermal and chemical stability, high hydrophobic nature, and favorable mechanical properties such as high yield modulus.

As reported in [41], depending if the polyimide is aromatic or non aromatic, the number of atoms of oxygen is various. So, if the presence of oxygen atoms is necessary for bonding polyimide film surface to the surface of other materials, such as PDMS with silane molecules, the aromatic polyimide would be a better choice. However, biocompatibility of aromatic polyimides has not yet been proved. Lower number of oxygen atoms can be problematic in cases that oxygen bonding is supposed to occur. As reported in [41], various

approached have been developed to ease this bonding including inter-diffusion of oxygen based materials as intermediate interfaces to gradually adapt the surfaces together, using an intermediate layer acting as an adhesive to bring the incompatible surfaces together, and bonding of plasma surface treated polyimide and PDMS as reported in [42].

2.4.4. Plasma Surface Treatment

Bonding or adhesion of polymers has been always a big issue. In our application, PDMS elastomer and PI are also among those materials which are not simply bond-able. For this reason, we should take special consideration to establish a durable bonding between these two materials.

Polymers should be chosen very accurately such that they have very excellent bonding properties, compatible to each other. Developing such materials that have very high bonding compatibility is very expensive. Surface preparation in bonding two distinct materials, however, can lead to a better bonding between two polymer surfaces.

Gas plasma treatment is one of the surface treatment approaches that recently has been used widely. As reported in [43] plasma treatment consists of a vacuum chamber, inside which the treatment process is conducted. Plasma treatment eliminates the barriers in bonding surfaces through three important effects that it has during this process. First, it removes the surface contaminations and weak polymer bonds. Second, by enhancing the adhesion of the resins on the surface of the polymers by incorporation of functional groups. And third, by formation of the functional group which permit the adhesion of polymer surface with resins. Since plasma treatment is a surface treatment, the properties of the bulk still remains constant.

Although almost all plasma devices have the same parts, there are still some differences among them which define their efficiency and functionality. These differences include power distribution, operational frequencies and gas dynamics. Depending on the materials that surface treatment is conducted on, any of these factors can change.

Diffusion of these active species including different types of gases, is very dependent on pressure; the higher the pressure, the shorter the mean free path is. The mean free path is the distance that active species can travel before undergoing collisions. Therefore, the concentration of active species varies either across the diameter of the chamber or between electrode pairs which apply the electricity. However, when working within the RF field, the gas is constantly being excited. Thus, polymeric particles being treated are exposed to a constant concentration of active species. In addition, plasma is rich in ultraviolet (UV) radiation, which is often an important starting step in polymer reactions.

According to the literature, plasma has different definitions. The most global definition is referred to another transition state of matter, when a liquid is exposed to high enough temperature changes its state to gas, and when this gas is exposed to sufficient additional energy, then it produces plasma. In case of gas plasma, it refers to creation of plasma when a gas is supplied with RF energy at reduced pressure. During this gas plasma process, the bulk material remains almost at room temperature.

Free electrons and metastable particles existing in plasma, collide with the surface of the polymer inside the plasma chamber and as a result break their covalent chemical bonds, producing free radicals on the surface. These free radicals can react with the gases and create new structure. This reaction may create new surface structure chemically which may be significantly different from the bulk material [44].

Plasma activation is the alteration of surface structure by the substitution of chemical groups for the groups normally present in the polymer chain. Within this mechanism the radical groups are establishing coupling with native gas inside the plasma. Depending on type of the gas selected for the process, a large variety of chemical groups including hydroxyl, carbonyl, carboxylic, amino, or peroxyl, can be created on the modified surface.

The strength of adhesion to a polymer is defined by four factors, as reported in [45-47].

(i) Removal of contaminations of the surface, which eliminates the intermediate layer between the polymer surface and adhesive and provides a condition that the surface and adhesive come to connect closely.

(ii) Increase surface energy of the polymer surface, which allows adhesive to wet the entire surface of the polymer.
(iii) Ablation of the surface, which increases the surface area between the adhesive and polymer.
(iv) Chemical manipulation of the surface, which improve covalent bonds between the polymer surface and adhesive.

Gas plasma produces all the conditions mentioned above, providing a strong adhesion between the substrate and adhesion. Evaporation of the surface material inside the plasma leads to removal of the intermediate layer between the substrate and adhesive. Actually, plasma provides a condition in which the molecular weight of the surface material decreases by scission of the chains, and these incomplete chains are enough volatile to be removed from the surface. Ablation of the surface also can occur inside the plasma when the surface of the substrate contains various material which react differently inside the plasma, so this difference in reaction can cause a surface become roughened.

In addition to the physical manipulation of the surface, plasma can also change the nature of the surface chemistry, so that prepares it for a stronger bond. This chemical effect happens when surface molecules react to the molecules of the plasma. Surface energy of the substrate can intensely increase by plasma-induced oxidation, nitration, hydrolization or amination. This higher surface energy increases the surface wettability and gives rise to a better adhesion. Another approach to increase this surface energy is to substitute the surface molecules with those that can build a covalent bonding with the molecules from adhesion. These modified groups of molecules are defined by the atoms in the plasma.

2.4.5. Aluminum Deposition and Thermal Evaporation

For deposition of thin metals on a polymeric material or on the surface of silicon, there are various methods of depositions which are basically divided into two categories of physical vapor deposition (PVD) and chemical vapor deposition (CVD) [48]. Each of these methods has specific features which makes it suitable for a specific materials or purposes. Different conditions including thickness of the metal deposited, purity of the metal deposited, alloys, thermal condition, etc. may define the suitability of one of the approaches.

PVD is usually used for thin film deposition (in our case thin Al film deposition on PI) when the purity of the metal deposited matters. In this method all the process is done inside a vacuum chamber, with very low pressure to eliminate obstacles for evaporation from the surface of the substrate. Different methods are used for evaporation of the source metals. Generally, three main techniques of PVD are available; sputtering, ion beam deposition and evaporation. In all three techniques the substrate is kept at room temperature. In sputtering, plasma is used for knocking off the source atoms, and in ion beam technique, the source is bombarded by an ion beam, while the pressure is remained very low. That causes the atoms of the source is separated from the surface and due to low pressure simply passes the way to reach the substrate.

Typically, two different methods are used for evaporation of the source material including thermal evaporation and Electron-beam (E-beam) evaporation. Thermal evaporation is one of the simplest and the most straight-forward way used for deposition of metals on a substrate. In this method, with resistive or inductive heating methods the source is heated up to its evaporation point. Due to very low pressure (0.1-1 μTorr) the metal atoms unbonded from the surface hit the substrate surface and make a bond to it. In a condition that higher temperature should be achieved for evaporating the source material, e-beam evaporation is used.

The illustrative figure of a thermal evaporator is shown in figure 2.8. The system is comprised of three main sections; a process chamber, a vacuum system and a metal heating system. Wafers are usually put upside down while rotating, to result in a uniform deposition. The metal to be deposited is placed inside the boat and heated to the vapor release point. Temperature inside the boat for vaporing the metal is between 500-2500 °C depending on the metal. Using a shutter, the process of evaporation on the substrate surface is controlled. By opening the shutter, evaporation starts, and it finishes when the shutter is closed. Using a quartz crystal, the thickness of the deposition is monitored.

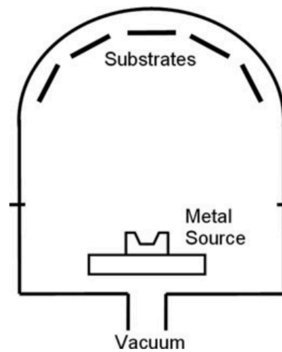

Figure 2.8. Illustration of a thermal evaporation system including main parts.

2.4.6. Etching

Generally speaking, etching is divided into two categories, regarding the effect that the etchant can have on the the substrate to be etched. These categories include wet etching, in which usually a liquid etchant is used and affects the molecular structure and bonding between the atoms of the material and etches it. Dry etching, which occurs in a dry ambient, and normally attacks the surface and removes the surface material by knocking them off from the surface, while chemical reaction is also expected.

Either wet etching or dry etching has limitations and benefits. There are many aspects that can influence selection of either of these etching methods, including type of materials to be etched, aspect ratio of the structure, selectivity of the material, intended uniformity of the structure, etch rate which is needed, etc.

From a different point of view, when etching uniformity matters, etching processes can be categorized into two groups of isotropic etching, and anisotropic etching. The difference between isotropic etching and anisotropic etching is illustrated in figure 2.9 [48].

In many MEMS structures, isotropic etching is a significant factor limiting maximum aspect ratio achieved. In fact, the higher isotropy of the etching process, the lower accuracy of the MEMS final structures is.

Figure 2.9. Difference between isotropic and anisotropic etchings, the brownish layer is photoresist.

However, even if wet etching is a highly isotropic process, due to its high selectivity, high throughput, and low cost, this method of etching is still commonly used, specially for structures which don't have high thickness. In structures with higher thicknesses, since the undercut of the structure can be significant when wet etching is used, so that this process is not very favorable.

Dry etching, in contrast, involves both isotropic and anisotropic features. A pure physical etching usually benefits from better isotropy, while selectivity is low. When a dry etching is occurred inside the plasma, due to the plasma gas, it involves chemical reaction with the material to be etched.

As previously discussed, for thicker layers of materials, when high aspect ratio is needed, wet etching is problematic. However, when a thin film is deposited on a substrate, if the line width of the structure is not so narrow, then wet etching process can be considered as a good choice for etching and patterning specific structures.

2.4.7. Aluminum Etching

Aluminum (Al) is a very light metal which has an excellent conductivity and low resistivity (28.2 n$\Omega.m$ at 20°C). Due to these remarkable properties, Al is commonly used in microelectronics as conductors. Furthermore, Al is not among noble metals family, the metals that resist against oxidation. So that, Al produces a very thin layer of aluminum oxidation (Al_2O_3) on its surface [49]. Because of this layer of oxidation, the normal tin/lead solders can not be used for the purpose of soldering aluminum.

In order to etch thin layer of deposited Al, wet etching can be used. This chemical etchant should involve 1-5% of HNO_3 for Al oxidation, and 65-75% H_3PO_4 for dissolving aluminum oxidation and 5-10% CH_3COOH for wetting and buffering and finally H_2O dilution to define the etch rate at a specific temperature. This etching process is highly isotropic, and extremely depends on the temperature.

Normally, developer solution used for Photoresist (PR) developing can also attack Al. For example, one of the developers which we also used in our laboratory for etching PR is TMAH-based developer (tetramethylammonium hydroxide, $C_4H_{13}NO$), which attacks Al with the rate of 50-100 nm/min.

3. DESIGN AND SIMULATION

We adopted polylactic acid (PLA) as a substrate and produced it by a desktop 3D printer. Our sensing cells are Al strain gauges formed on the surface of a thin polyimide sheet. A layer of cured PDMS is also used to support this polyimide film and contacts the object for tactile sensing. Since our vibrotactile system has moving probes for stimulation [8], we used a flat contact surface instead of bumps on the surface of the sensor.

In this section design concepts and results of simulation with COMSOL are presented, and then the comparison between simulation results and mathematical calculations are demonstrated.

In order for the sensor to have maximum sensitivity, and for concentrating maximum stress applied by the tips of the vibration system on a small area, the sensor was designed based on array of membranes. The physical principle of this sensor is based on the distribution of stress and thus strain on a rectangular membrane which is under normal stress as discussed in section 2. The intensity of the stress is higher at the center of the periphery. Furthermore, if one surface of the membrane faces normal tensile stress, this stress values drops down linearly in the direction of the thickness of the membrane; it becomes zero at the neutral plane. The remaining half of the membrane experiences compressive stress which increases linearly, and reaches its maximum value on the surface of the other side [50]. Thus, the most appropriate regions for sensing the stress is either in the top surface of the membrane or the bottom one. In addition, choosing an area of the periphery on which the highest value of the stress is concentrated is essential for placing the strain gauges. If the strain gauges are placed on the area of the periphery that experiences highest amount of stress, then the sensor experiences higher sensitivity.

3.1. Comparison of Mathematical Calculation and Simulation Results

To calculate the value of stress appeared on the surface of a square membrane clamped in the edges, usually numerical analysis such as finite element or finite-differential methods, or approximate mathematical analysis such as energy method is used, as we discussed in

section 2. In order to observe the distribution of stress in the surface of PI membrane used for sensor, equations 2.15, and 2.16 are used. By substituting the values shown in the table 3.1, the 3D graph of the equations was obtained in MATLAB. We assumed that the pressure is a distributed load on the surface of PI membrane. Since the radius of the probe used for applying pressure is almost the same as diagonal of the square membrane, then we expect the results should be close the ones we will experience in experiments.

Table 3.1. Values for calculating stress on a membrane.

t	125 μm
ν	0.34
a	1.25 mm
F	2 N

The plots in figure 3.1 shows the results. These plots show stress distribution on the bottom surface of PI membrane, when the distributed force, q (F/A) is applied on the top surface. As shown in this figure, the concentration of the stress in both x and y directions are highest around the center of each edge. Therefore, the best place where the strain gauges are exposed more to stress is around the center of each edge. The maximum and minimum of the stresses are shown in z axis in both plots in figure 3.1.

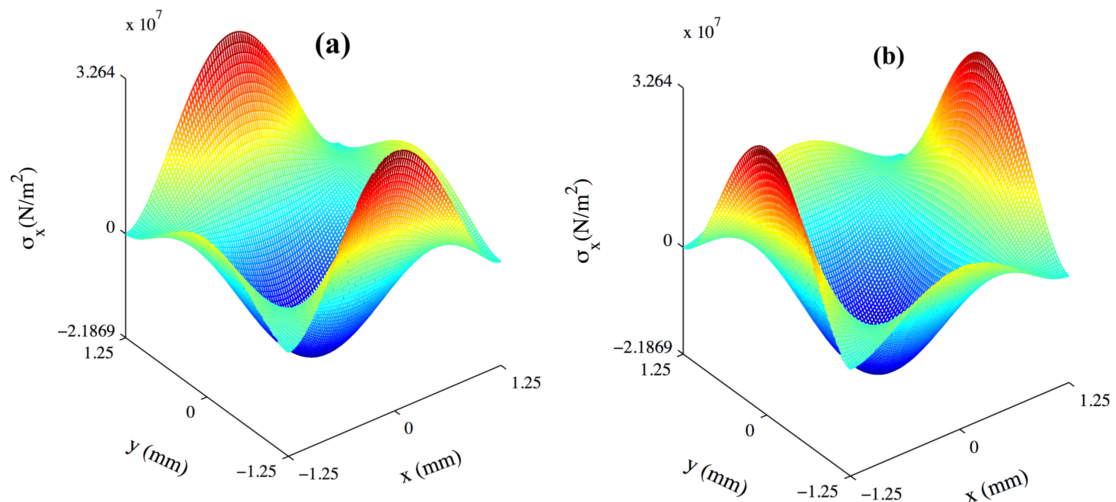

Figure 3.1. Plane stress on the bottom surface of PI, derived by approximate equations (a) stress distribution in x direction (b) stress distribution in y direction.

Based on the equations, the intensity of the stress on the surface of the membrane is also dependent on the thickness, length and mechanical properties of the material. Thus, in order to obtain higher sensitivity, all these variables should be considered. Another aspect that the design of the sensor is highly affected by is the capability of the sensor to tolerate higher deflections. For this purpose, PDMS layer has to be thick enough to handle this high deflection, with this consideration that higher thickness leads to lower sensitivity of the sensor.

To evaluate the stress distribution results obtained by approximate equations, a static simulation was run in COMSOL Multiphysics. For this purpose, the structure that we used was the same as the one we used to obtain approximate results. The same structure was simulated in COMSOL. As illustrated in figure 3.2, the simulation results proved the results we observed in the numerical calculation.

According to the analytical and simulation results, stress depends on multiple factors besides loading conditions such as geometrical variables and mechanical properties. Therefore, to obtain higher sensitivity, all these variables should be considered in a simulation. To investigate the effect of PDMS thickness on stress on PI membrane, a simulation was performed with PDMS of two different thicknesses (1.2 mm and 1.7 mm) placed on a PI layer. Figure 3.2(c) shows the results of this simulation. As we expected based on previous analyses [50,51], the simulation demonstrates that the thicker PDMS layer leads to a lower intensity of stress in the middle of the edges on the PI membrane when the same displacement (0.5 mm) was applied on both PDMS layers.

An important design consideration is the nominal resistance of a strain gauge. The resistance change due to strain is proportional to the nominal resistance [50]. Therefore, to achieve higher sensitivity, the thickness of the Al deposited on the PI membrane may be reduced. However, thickness below 50 nm increase the risk of damage during use. To increase the sensitivity further, we placed 4 strain gauges in series for each cell, placed at the midpoints of each edge as explained earlier. A constant current was driven through this series circuit, and the voltage across the circuit was measured. Since we did not use a Wheatstone bridge and our stimulator probes were large (2 mm), asymmetric loading was not problematic in our application. If a probe was offset relative to a given cell, the main

effect would be to decrease the sensitivity for that channel. However, due to the redundant multi-channel approach, another probe may be closer to a different cell and enable a higher reading from its channel. There are 230 probes moving all together in our stimulator.

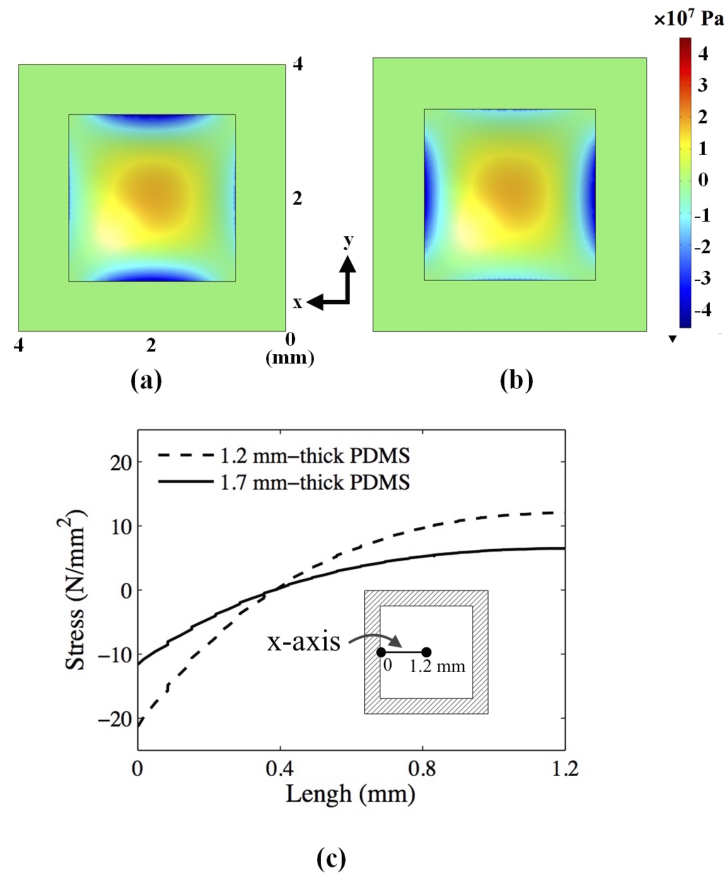

Figure 3.2. (a) COMSOL simulation results showing stress distribution (in y direction) on the bottom surface of a 0.125-mm-thick PI membrane when a distributed force was applied on the top. (b) Same as in (a) with stress distribution in x direction. (c) COMSOL simulation results of stress distribution on PI membrane with a PDMS layer on the top. The results are given along the x direction when a static displacement of 0.5 mm was applied on the top of PDMS layer. PI thickness was the same for both membranes. PDMS thicknesses was 1.2 mm for one, and 1.7 mm for the other. The inset shows the measurement axis [65].

In order for the sensor system to acquire force information at different locations simultaneously, we designed an array of sensing elements. Although the output from each sensing element is processed separately by the processor in figure 1, the sensing elements would not contain independent information in our operant chamber which has all the probes

moving together [8, see figure 1]. This approach was deliberate to allow the stimulation of the skin or the sensor regardless of the animal's location in the chamber. The geometry of the chamber and sensor design ensure that several probes always contact the sensor surface while the rat is performing the psychophysical task. Nevertheless, considering the possible use of a similar tactile sensor in a different operant chamber, we still attempted to reduce the cross-talk between the neighboring cells by allowing a sufficient distance between the cells and conductive traces [52,53]. As a result, the sensor consisted of a 2×7 array of sensing cells with 2.5×2.5 mm^2 square cells (Figure 3.3). Two of these elements are saved for temperature compensation, so their cells do not have cavities to allow deformation. The PDMS layer was designed at different thicknesses (1.2 and 1.7 mm) in two prototypes to test its effect on the sensitivity. Mechanical forces of bonding between the substrate, polyimide sheet and PCB establish electrical interconnections between the sensor pads and PCB. Sufficient distance between each individual cell and their independent functionality remarkably lower cross talk between neighbors.

3.2. Dynamic Simulation of Sensor

In order to investigate dynamic response of a membrane of the sensor, a simulation with the same materials as we used for the fabrication was done in COMSOL. One of the membranes with the same dimensions mentioned above was taken for the simulation purpose. Properties of the materials used for COMSOL simulation is presented in table 3.2.

Table 3.2. Properties of the materials used for simulation purpose.

	density (kg/m^3)	Poisson’s ratio	Young’s modulus (Pa)
PI	1420	0.34	2.5 G
PDMS	970	0.499	0.35 M

In order to calculate an approximate value for resonance frequency of the membrane, we used the equation 2.24. For this purpose, spring constant of the structure is needed. To obtain an estimated value for spring constant of the membrane, we assume the membrane as a system of spring-mass-damper. When a force is applied from the top, we assumed the central deformation as the deformation of the spring. For calculating the central deformation in a membrane, we used equation 2.14 at the center of a membrane. In addition, since our

system doesn't experience any squeezed damping effect, we consider the value of the damping coefficient is zero. With these assumptions, the natural frequency of the system is its resonance frequency.

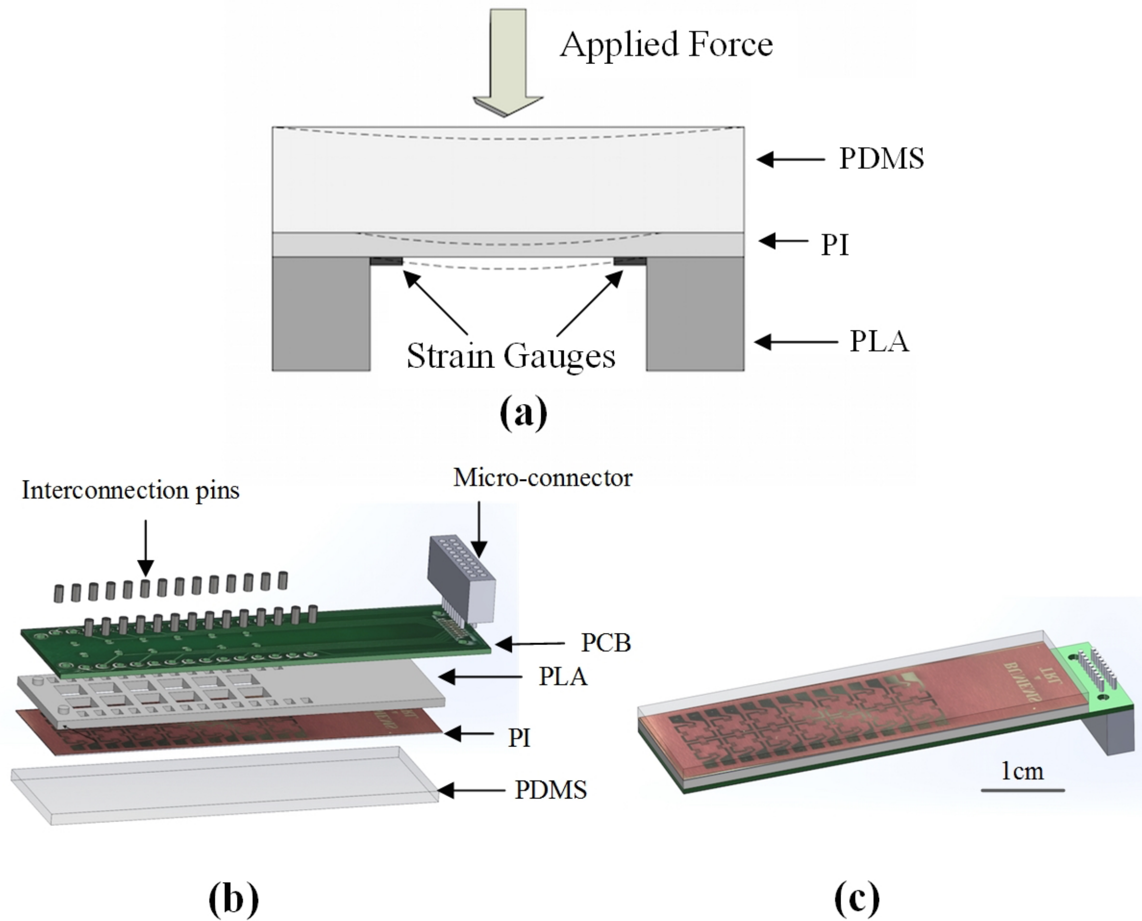

Figure 3.3. (a) The cross-sectional view of a cell and the direction of applied force. (b) The components of the sensor were designed in Solidworks. (c) 3D graphical view of the assembled sensor [65].

Using the values presented in table 3.2, the spring constant and resonance frequency of the PI membrane is obtained. Resonance frequency of a membrane is presented in table 3.3.

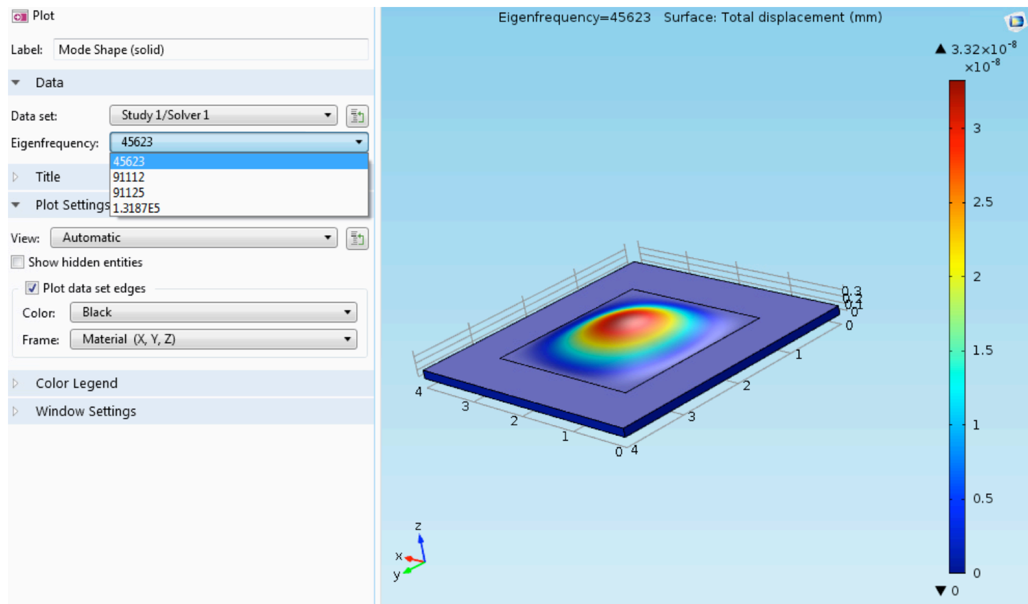

(a)

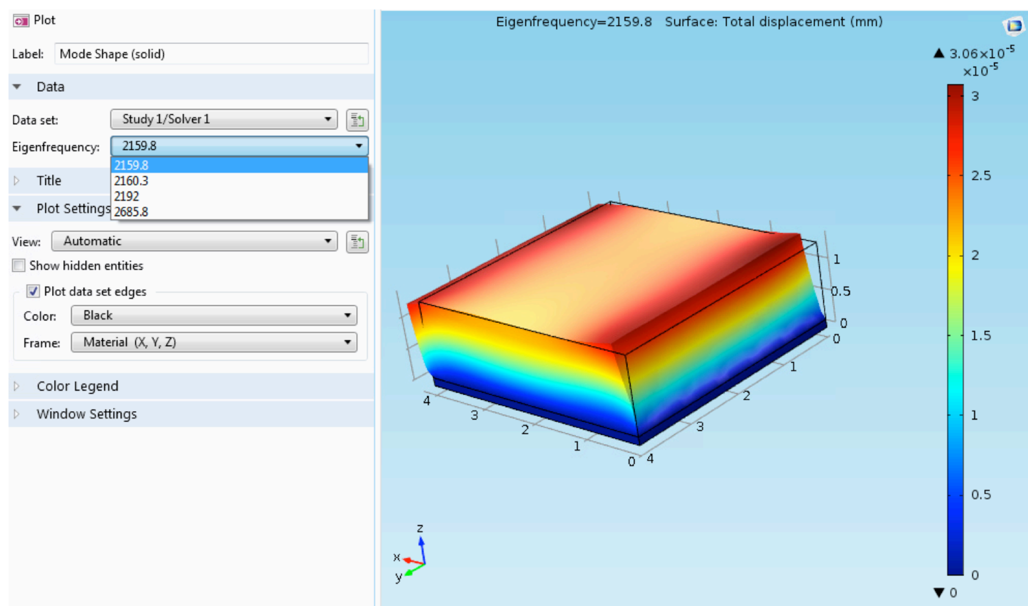

(b)

Figure 3.4. Results of dynamic simulation of the membrane in COMSOL (a) resonance frequency of the membrane without PDMS, (b) resonance frequency of the membrane with 1.2 mm-thick PDMS bonded to the PI surface.

Figure 3.4 shows the structure and its resonance frequencies obtained by dynamic simulation in COMSOL. As observed in this figure first resonance frequency of the structure is close to what we calculated using an approximate method.

However, we expect with using a layer of PDMS on top of the PI membrane, spring constant of the structure will drop dramatically and consequently the resonance frequency will decrease by a large amount. So, to make sure if the bandwidth of the membrane with PDMS is still in an acceptable range, we did another simulation with 1.2 mm-thick PDMS on top of PI. The results of this simulation are presented in figure 3.4(b). As we expected, a huge decrease in resonance frequency is observed. However, still the resonance frequency is far from the frequency range in which the experiments are conducted.

In table 3.3, the results of both approximate calculation and COMSOL dynamic simulation of PI membrane are presented.

Table 3.3. Spring constant and resonance frequency of the membrane acquired in approximate calculation and simulation.

	calculation	simulation
f_r (Hz)	41.5k	45.6k

4. FABRICATION

The fabrication of the sensor array includes four main steps: patterning of the strain gauges on a PI sheet, PDMS preparation, substrate fabrication using a 3D printer, and integration of all the components. Figure 4.1 shows the various layers prepared during the fabrication process.

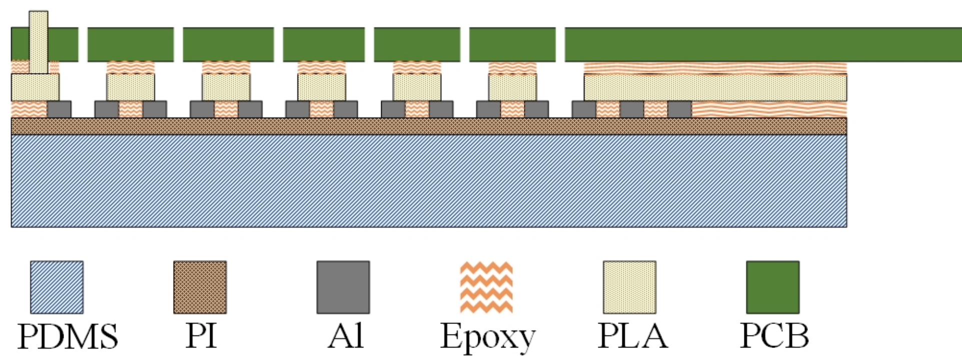

Figure 4.1. Cross-sectional view of the sensor system shows all its layers prepared during the fabrication [65].

4.1. Strain gauge patterning

The first step in the fabrication process was the formation of Al strain gauges on a PI sheet by using a single mask (shown in appendix A). PI has properties which makes it suitable for our purpose, as explained in section 2.4.3. So, A 125-μm thick Kapton HN PI sheet was used. After cutting and trimming the edges of the sheet, acetone and isopropyl alcohol (IPA) was used to wash away oil and small particles from the surface. The surface was then rinsed by deionized water (DI water), and dried under N_2 stream. Using high vacuum thermal evaporation with precise deposition rate control, a thin layer of 50 nm Al was deposited on the PI surface. Following this, the Al surface was spin coated with a thin layer of photoresist (PR) film. The strain gauges were patterned on the PI surface by standard photolithography and etching. We used tetramethylammonium hydroxide (TMAH) based AZ 725 MIF developer to etch the Al layer. This TMAH-based developer solution can be used for both developing the PR film (~ 1 min.) and etching the Al layer (~ 1 min.), as described in section 2.4.7. Afterwards, the sheet was cleaned with acetone to remove the

remaining PR from the surface, rinsed with IPA and DI water to remove the acetone, and finally dried by blowing N_2. Various steps of the fabrication process are shown in figure 4.2.

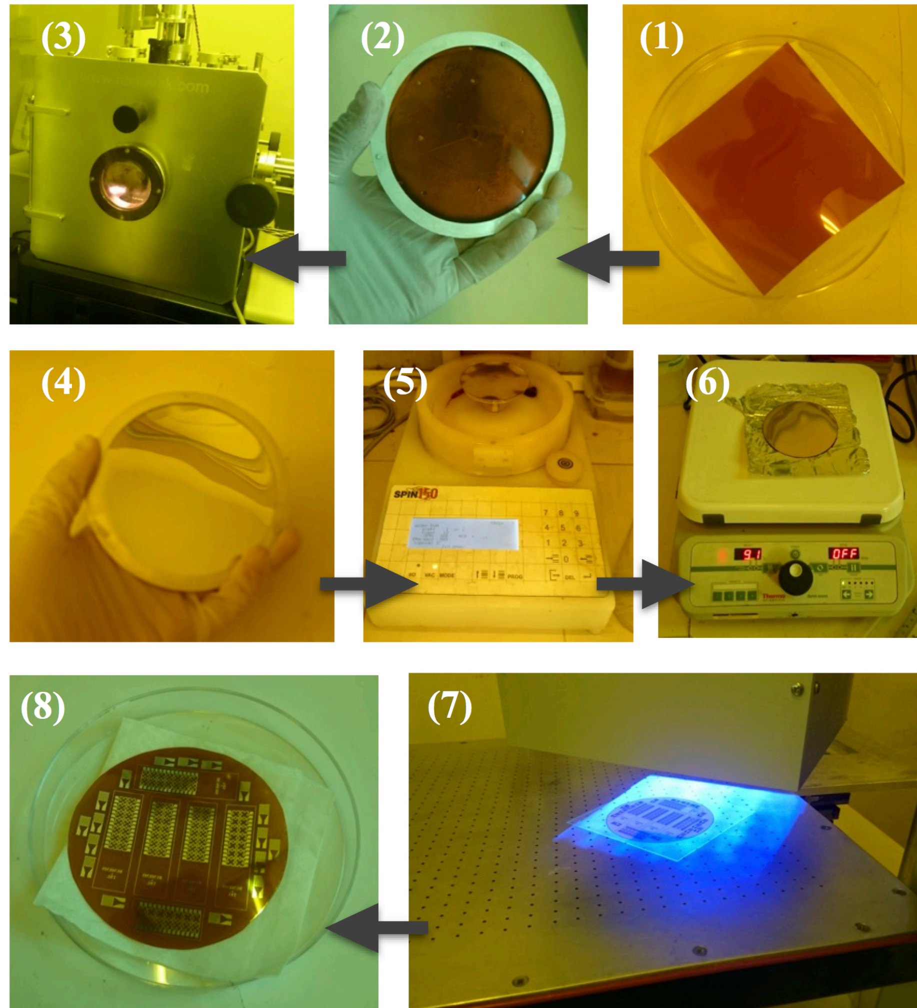

Figure 4.2. Steps in fabrication of Al strain gauges on PI sheet. (1) PI sheet before cutting and trimming, (2) Trimmed PI sheet installed in the metallic holder of the evaporation chamber, (3) thermal evaporation chamber, (4) Al deposited on PI sheet, (5) PR coating on PI sheet, (6) heating coated PR for hardening, (7) Photolithography by UV, (8) final product of the sensor layout after etching and removing the etchant and PR.

4.2. PDMS and substrate preparation

Two PDMS sheets with different thicknesses (1.2 and 1.7 mm) were prepared by using Sylgard 184 Silicone Elastomer Kit. The elastomer and the curing agent were mixed with a ratio of 10:1. The prepared mixture was applied to plastic molds, and left untouched for one day at room conditions. We ensured that the mold was placed on a level surface to obtain PDMS samples with uniform thickness. The PDMS sheets were cured on a hot plate at 90°C for 15 minutes after peeling off. Finally, they are washed with IPA, and dried under N_2 stream. Figure 4.3 shows the PDMS sheet peeled off from the plastic container.

Figure 4.3. PDMS sheet peeled off from the plastic container after one-day cure in room condition.

We designed the substrate with Solidworks (Dassault Systèmes; Waltham, MA, USA). 14 square-shaped 2.5×2.5 mm^2 cavities were patterned on a 45×14×1 mm^3 rectangular prism. The thickness of the substrate was selected to allow the deflection of the PI cell membrane without causing any squeeze-film damping. In addition, some vias through the substrate were opened for inserting metal pins, which were used for electrical interconnection between the PCB pads and the Al strain gauge pads. The substrate was made in MakerBot Replicator2 3D printer (Makerbot; Brooklyn, NY, USA) by using PLA material. To establish the electrical connections, a 0.6-mm-thick PCB was used. It had traces and pads for attaching

an Omnetics Nano Strip connector (model A79014-001; Omnetics Connector, Minneapolis, MN, USA).

4.3. Sensor integration

For the integration of all sensor components, the PLA substrate was initially bonded to the PCB by epoxy resin. A strong adhesion was formed by applying 2-kN force under a vise for 20 minutes. It took 2-3 hours for the epoxy to be fully cured at room temperature. Heating was not applied, because PLA has a low melting point of around 115 °C. Next, the back side of the PI sheet was joined to the PDMS layer. Bonding PDMS to other polymers is challenging due to very low surface energy of PDMS and its hydrophobic nature, as we discussed earlier in section 2.4. However, different direct and indirect methods have been reported [54-56]. We coated the backside of the PI with epoxy. Prior to attaching PDMS to the polyimide sheet, the surface of the PDMS was activated by using oxygen plasma for 1.5 min. After joining two surfaces and applying a 4-min. cure on a hot plate at 100 °C under low force (200 N), a strong bond was formed.

For bonding the PLA substrate surface to the PI surface, the accurate alignment of the strain gauges with the cell cavities is very essential. Alignment error may lead to different sensitivity values for different strain gauges. Before two surfaces came to contact, the PLA surface was coated with epoxy, and then two surfaces were joined using a custom-made aligner system under microscope. The surfaces were held in contact for 30 min. for a stronger and durable bond. After releasing the aligner, it took 2-3 hours for a fully-cured bond. The micromanipulator in our alignment system has 10 μm resolution in the xy-plane and 1 μm resolution in the z-direction. The maximum alignment error was kept less than the designed distance (50 μm) between the strain gage traces and the cavity edges of the PLA substrate.

Finally, electrical interconnections between the Al pads on the PI surface and the PCB pads were established through the vias of the PCB and PLA. Direct mechanical pressure was found to be more reliable for connecting copper pads on PCB to the Al pads on PI. Copper header pins were inserted through the vias and they made electrical contact with the Al pads. The other ends were soldered on the PCB pads. A micromanipulator and a precise digital balance were used to apply the same mechanical force that results in good electrical

connection to the pins while their soldering are done to the PCB. As the last step, the Omnetics connector was soldered on the PCB. Figure 4.4 shows both the fabricated sensor array and a single strain gauge patterned on the surface of the PI sheet.

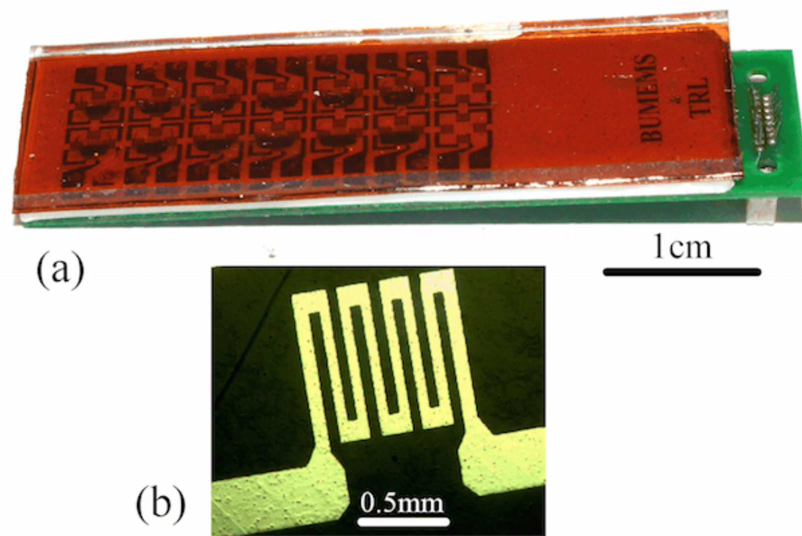

Figure 4.4. (a) Fabricated sensor array. (b) Magnified photograph of an Al strain gauge patterned on the PI layer [65].

5. CHARACTERIZATION AND TEST

Two different setups were used for the static and dynamic characterization of the sensor elements in the tactile sensor. Cross-talk was measured in the static condition. Additionally, the sensor was tested in the operant chamber designed for the tactile neuroprosthesis.

5.1. Static Characterization

To calibrate the static response of the tactile sensor, a micromanipulator, a precise digital balance (Kern 440; Kern & Sohn, Balingen, Germany), and a semiconductor DC characterization system (Keithley 4200SCS; Tektronix, Beaverton, OR, USA) were used. The sensor was attached to the weighing platform of the digital balance. By using the cylindrical micromanipulator probe (diameter: 1.7 mm), a controlled displacement/force was applied on the center of each cell. The displacement could be controlled at 10-μm resolution by the fine-scale adjustment knob of the micromanipulator. The calibration probe could be positioned on each cell with 10 μm accuracy. Since the micromanipulator was used on a vibration-isolated optical bench, vertical alignment was maintained. Figure 5.1 shows the the system used for static characterization. The nominal value of each sensor cell's resistance, combination of four in series, was approximately 280 Ω.

Simultaneous to the displacement control and measurement, the applied force could be measured at mN resolution by the digital balance. The displacements were tested in the range of 100-900 μm. During static loading, a constant current of 1 mA was applied to the series combination of 4 strain gauges in the cells and its voltage changes were recorded by the DC characterization system (a set of recorded signals are presented in appendix B.1). The calibration was performed three times on three different cells, and the data were averaged for each of them. Results were obtained from tactile sensors with two different PDMS thicknesses. Figure 5.2 shows the average change in resistance as a function of displacement and force in two exemplary sensing elements, from tactile sensors with different PDMS thicknesses.

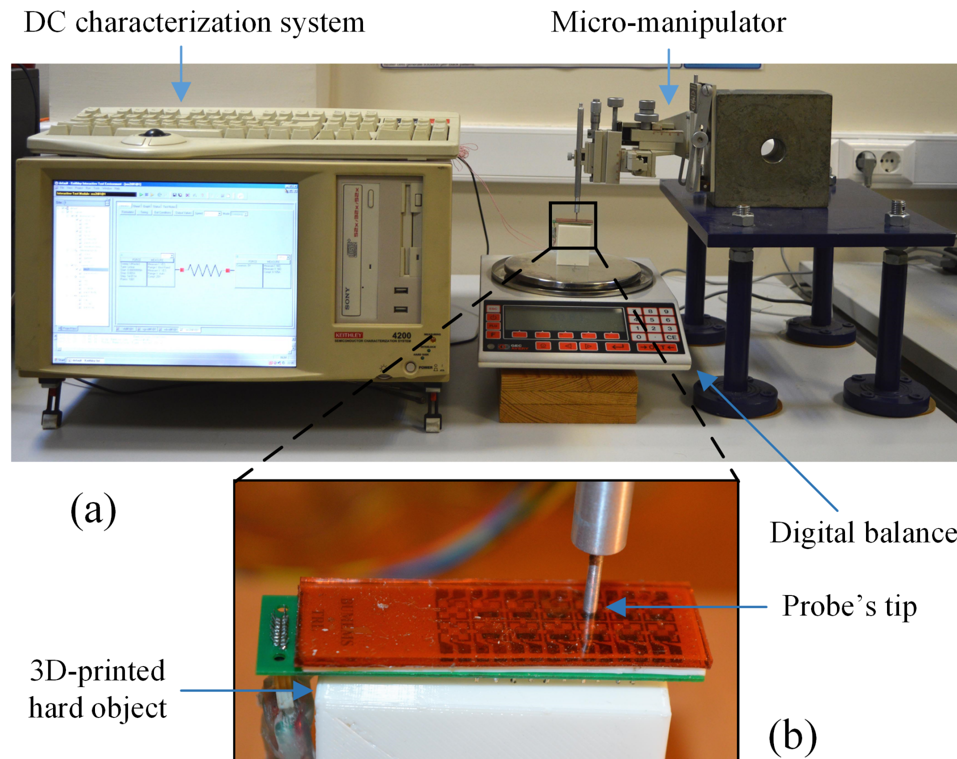

Figure 5.1. (a) The system used for static characterization of the fabricated sensor, (b) a magnified photo of the sensor installed on a 3D printed stand, while the cylindrical probe is pressing at the center of a membrane in the array.

According to the characterization results, the sensors could detect forces with maximum intensity of 3-4 N, at a sensitivity of 70-200 mΩ/N (0.3-0.7 Ω/mm), and nonlinearity of 3%. The stiffness of the sensors is 4000 N/m for 1.7 mm-thick PDMS and 3000 N/m for 1.2 mm-thick PDMS. These values also include the contribution of 0.125 mm-thick PI membrane.

To measure the cross-talk in a sensor with 1.2 mm PDMS thickness, force was applied to the neighboring cells of the sensing cell from which the resistance change was measured (Figure 5.3(a)). The test was repeated for three neighboring cells in different positions of the array, and then the data were averaged. The slope of the resistance change showed that the cross-talk was approximately 5 mΩ/N (0.02 Ω/mm), which is much lower than the sensitivity of the sensing elements (Figure 5.2(a)).

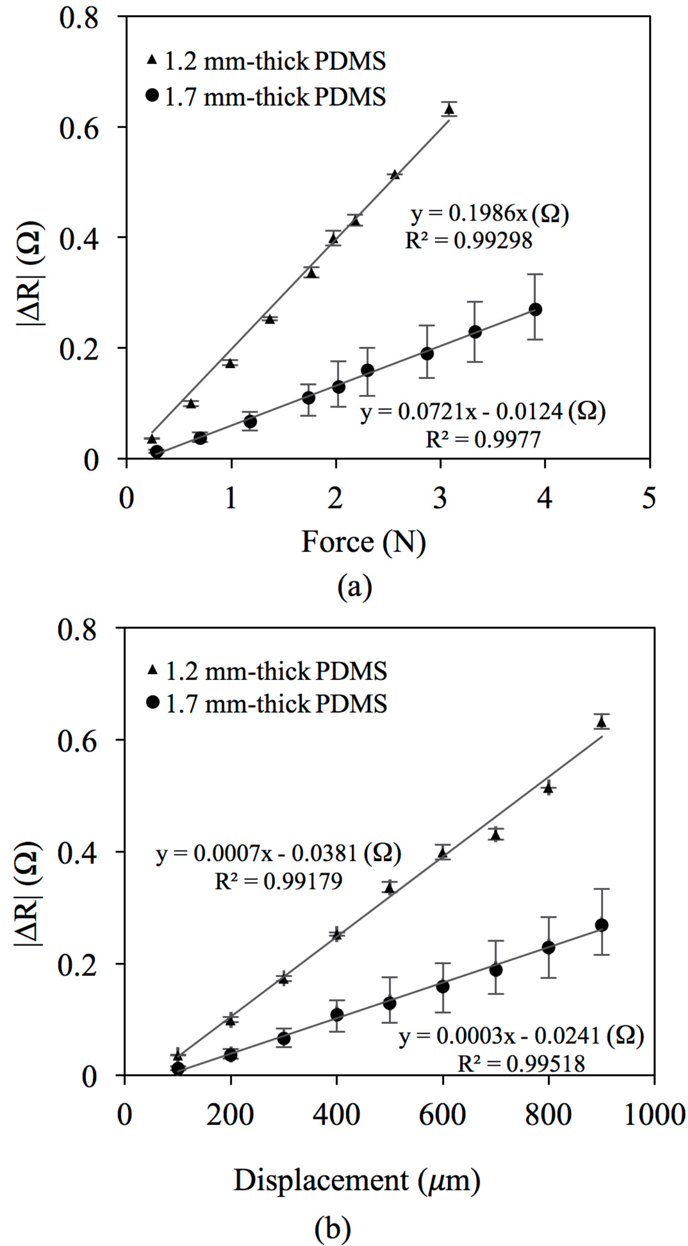

Figure 5.2. Static characterization results of the fabricated sensors based on (a) force and (b) displacement applied to the surface of the PDMS [65].

We also measured off-center sensitivity of one cell in two directions as depicted in figure 5.3a. The data from two directions were averaged. As can be seen in figure 5.4, there is a slight decrease in the resistance change 1 mm away from the center, but the sensitivity (slopes of the curves) is similar to that in the center. However, the resistance change and sensitivity both decrease significantly at 2 mm and 3 mm away from the center.

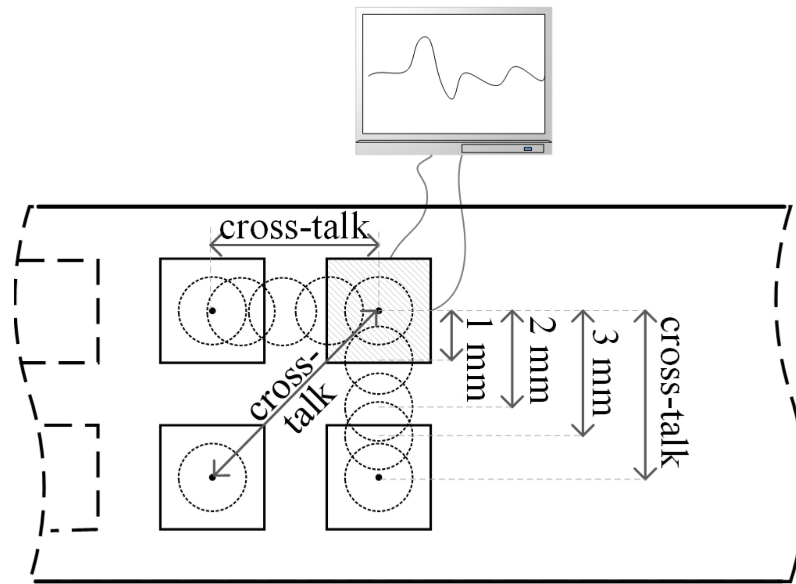

(a)

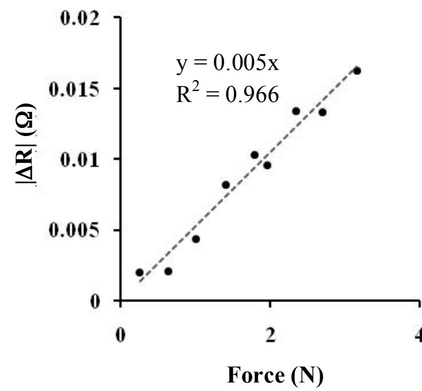

(b)

Figure 5.3. Cross-talk measurements. (a) Diagram for cross-talk and off-center measurements. The scope trace shows the cell from which recording was made. Probe locations are shown by circles. (b) The data show the average resistance change in one cell with 1.2 mm thick PDMS film when the probe was positioned on neighboring cells [65].

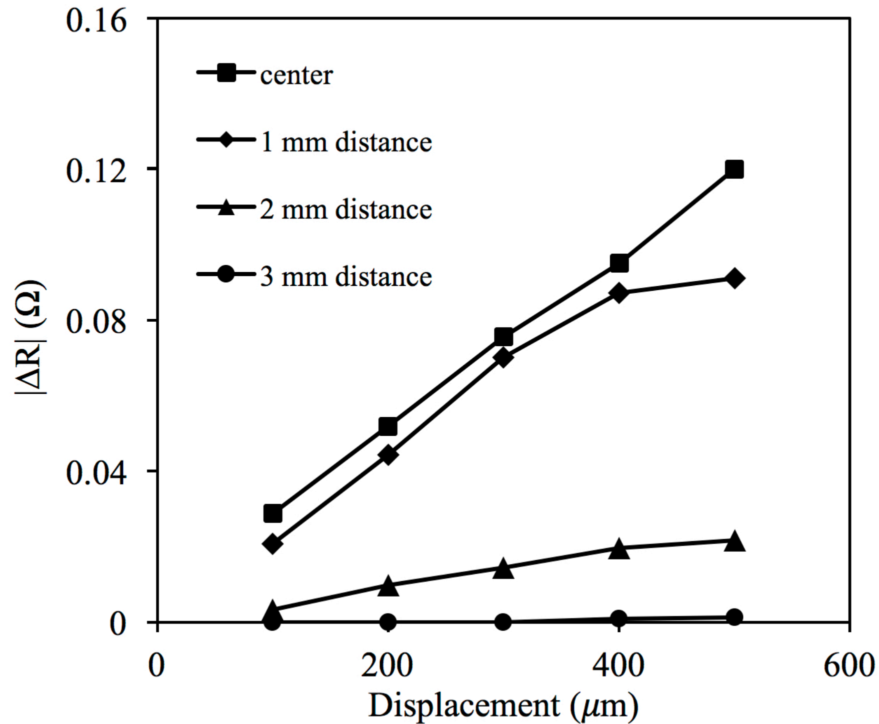

Figure 5.4. Effects of probe distance on resistance change and sensitivity for cells with 1.7 mm thick PDMS film. The probe locations are off-center and are depicted in figure 5.3(a) [65].

5.2. Dynamic Characterization

For characterizing the dynamic response, a vibrotactile stimulation system was used [57-59]. This system consists of an electrodynamic shaker (LDS V201; Brüel & Kjær, Nærum, Denmark) for mechanical stimulation, a digital attenuator (PA5; Tucker-Davis Technologies; Alachua, FL, USA) for adjusting stimulus levels, and a power amplifier (Alesis RA300; inMusic Brands, Cumberland, RI, USA) for driving the shaker. The sinusoidal stimulus waveforms were generated on a PC running MATLAB, and output by a digital to analog converter card (IOtech DaqBoard/2000; Measurement Computing, Norton, MA, USA). The sensing cells were supplied by 1 mA constant current sources based on a LM334 integrated circuit. The voltages across the sensor cells were amplified (gain: 10k) by an AC biopotential amplifier (DAM50; World Precision Instruments, Sarasota, FL, USA), and the amplified sensor output was acquired by an analog to digital converter (IOtech DaqBoard/2000). Using custom-made software in MATLAB (MathWorks, Natick, MA,

USA), sinusoidal vibrotactile stimuli were generated at predefined displacement amplitudes (10-300 μm) and frequencies (2-500 Hz), and the amplified sensor-output waveforms were recorded on the computer. The frequency range was selected based on the tactile sensitivity of mammals [60,61]. To emulate skin-contactor coupling, the vibrations were superimposed on a static indentation of 0.4 mm. Figure 5.5 shows the entire system.

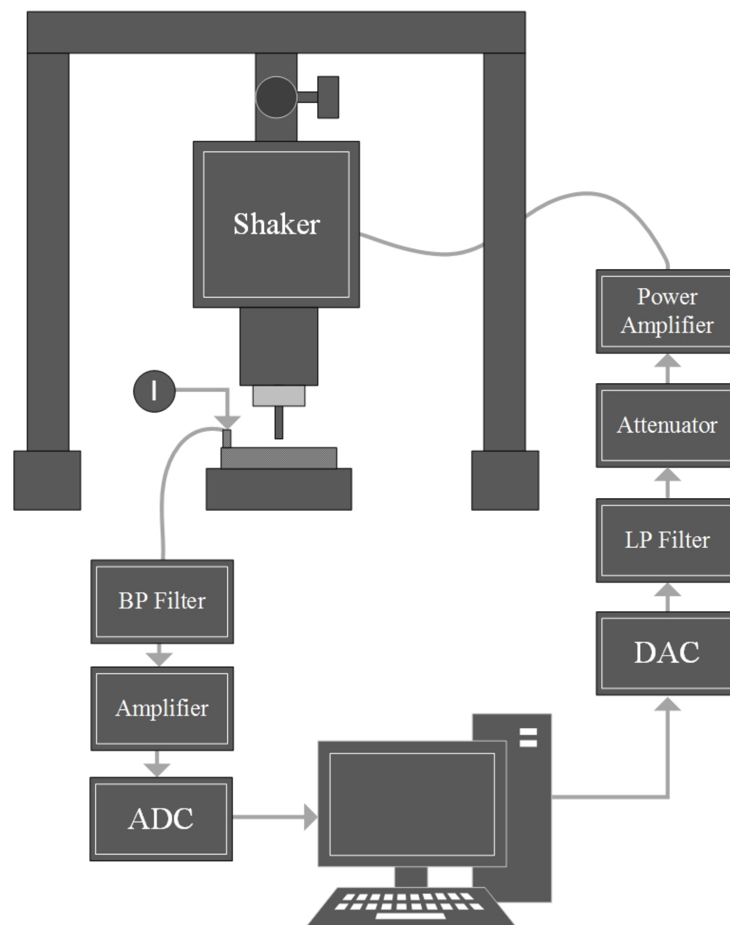

Figure 5.5. Tactile psychophysics setup used for the dynamic characterization of the sensor array [65].

The amplified voltages from the sensor elements were superimposed on the background noise of the data acquisition system. Therefore, saved waveforms were analyzed by FFT offline. Figure 5.6 shows the output from a sensor element in dB units (referenced to 1 Vrms before amplification) as a function of frequency, and the mechanical input level as the parameter. Different displacement inputs from 10 μm to 300 μm are given in zero-to-peak micrometer units. Nine frequencies of mechanical vibration (2-500 Hz) were tested (the

result for mechanical vibration with frequency of 5 Hz and amplitude of 150 μm is shown in appendix B.2). Due to the limitation of the vibrotactile system at high frequencies, 300-μm displacement amplitudes could not be generated at 500 Hz. The frequency response is flat within 7-15 dB in the tested range. Furthermore, it can be observed in figure 5.6 that the sensitivity is very similar at each frequency. In other words, the vertical spacing between the data points are alike. This shows good linearity in the dynamic response.

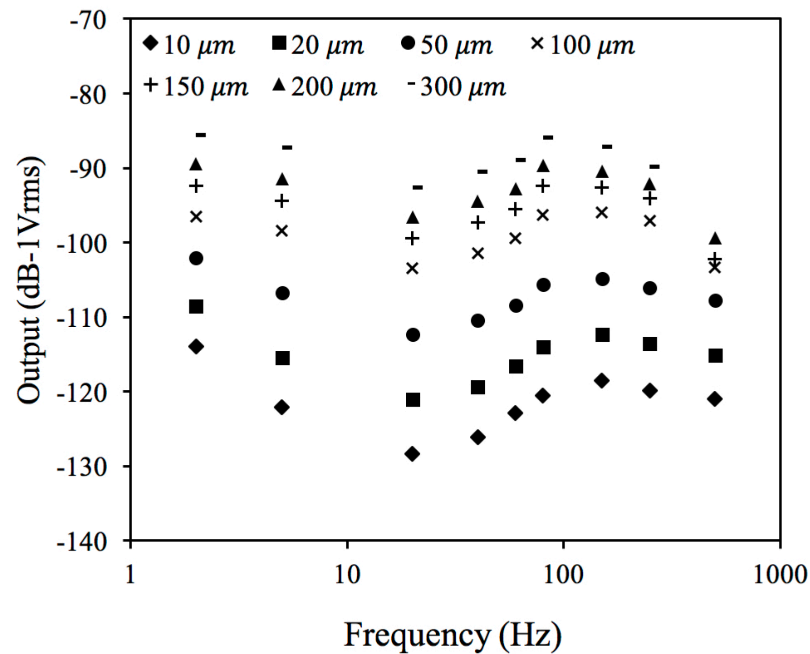

Figure 5.6. Dynamic characterization results of one sensing element in the range of 2-500 Hz and at different displacement amplitudes [65].

5.3. Sensor Test

To test the sensor in the operant chamber [8], we placed it on the ground plate as shown in figure 5.7. The plate had holes through which stimulator probes moved. After adjusting the static indentation to 0.4 mm, 80-Hz sinusoidal vibrations with zero-to-peak amplitudes of 50 and 200 μm were applied to the tactile sensor. The output from a sensing element which had direct contact with a stimulator probe was amplified as described in the previous section.

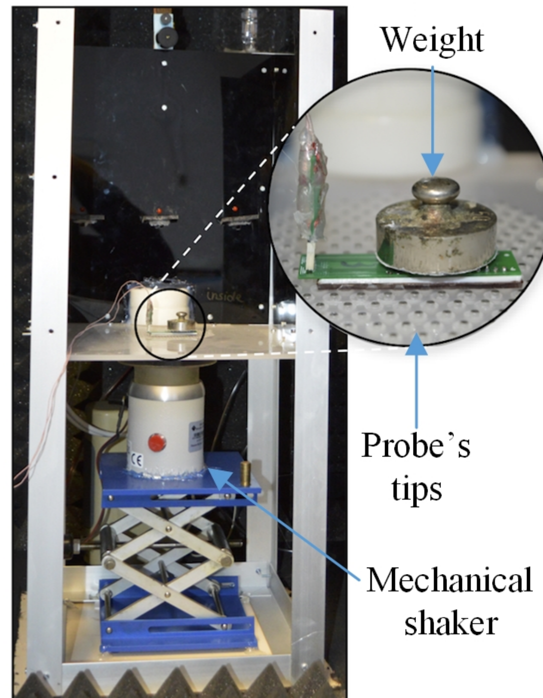

Figure 5.7. Side view of the operant chamber with the sensor array placed on the ground plate. The vibrotactile stimuli are applied with the probes which move through the holes in the plate [65].

Figure 5.8 (a) shows the signal which is generated to drive the shaker. As the sensor was placed on the stimulator probes, the surface of the sensor is stimulated and the output voltage signal which is sent to the DAQ card is shown in figure (b). After offline, digital filtering in MATLAB (figure (c)), and by using the data driven in sensor calibration, displacement amplitudes are obtained (figure (d)). Based on some experimental models on rats, and by using envelope detection of the acquired signal, the ICMS pulses were generated. In brief, corresponding vibrotactile stimulus amplitudes and ICMS current amplitudes produce similar hit probabilities in detection tasks. Therefore, the psychophysical equivalence function maps a given mechanical displacement amplitude to an electrical current amplitude [65].

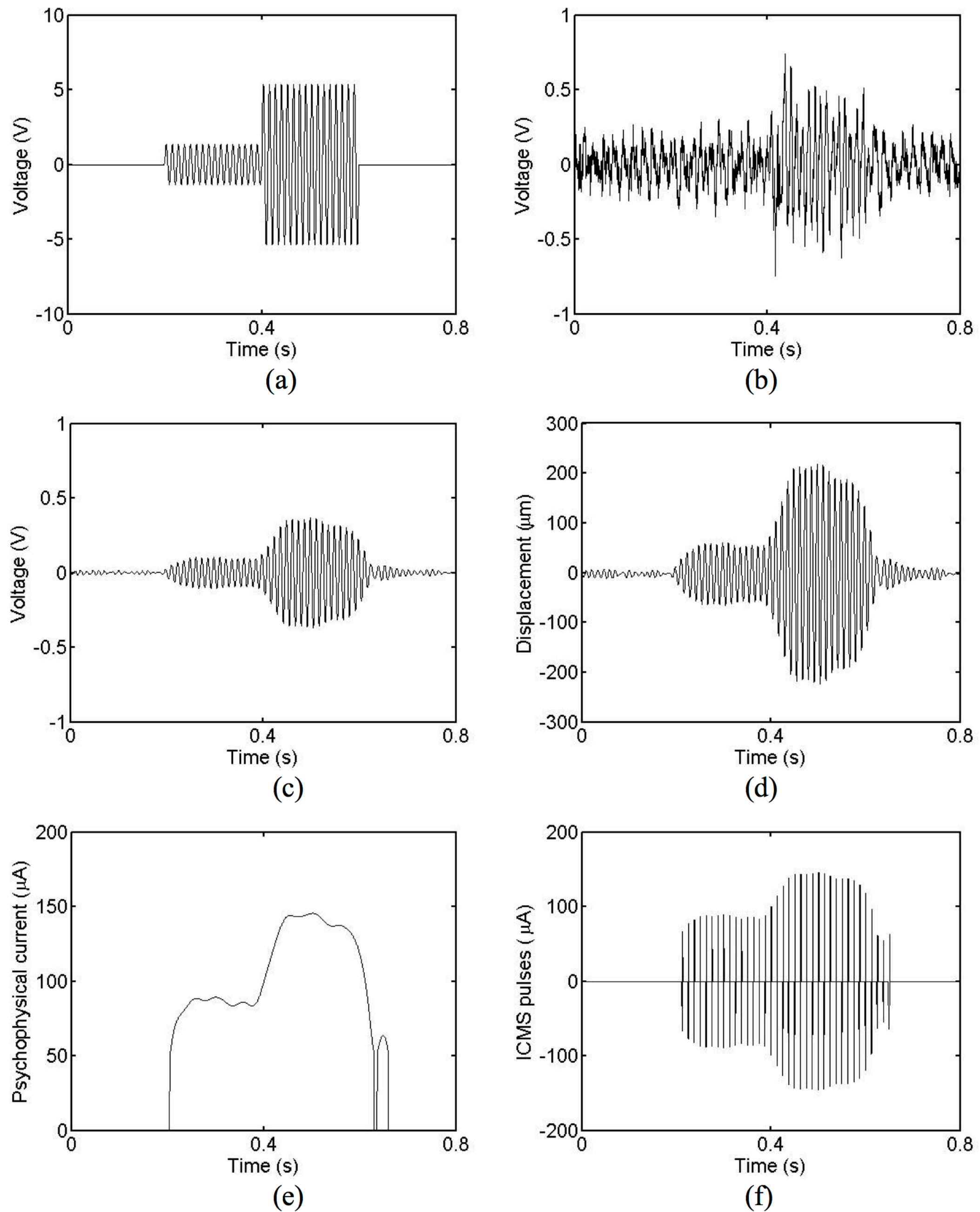

Figure 5.8. Results from the rat operant chamber show the relevant signals in a tactile neuroprosthesis. (a) Command signal for the mechanical shaker. (b) Amplified signal from one channel of the tactile sensor. (c) Band-pass filtered sensor signal. (d) Displacement signal based on sensor calibration. (e) Envelope of the electrical current with equivalent psychophysical performance. (f) ICMS pulses for applying to the somatosensory cortex in the rat brain [65].

The ICMS waveform, i.e. signal F in figure 1, was obtained by a special form of pulse amplitude modulation. The waveform for each pulse was similar to that is used in rat experiments. It was biphasic (cathodic phase first) with phase duration 600 μs and an inter-phase interval of 50 μs. The current pulses were simulated with the same frequency, here 80 Hz, as the vibrotactile stimulus frequency. This is the standard ICMS frequency protocol used in our experiments. The envelope signal (figure 5.8(e)) modulated the zero-to-peak amplitude of the biphasic ICMS pulses resulting in the waveform given in figure 12f. It is important to note that ICMS should be applied in current-controlled mode [62,63], because electrode-tissue impedance changes with time. In figure 5.8, the sensor output was recorded for a 0.5-s epoch and processed subsequently. Ideally, the ICMS pulses will be applied simultaneously as the tactile stimuli are presented.

6. DISCUSSION AND CONCLUSION

In this study, we presented the design and microfabrication of a tactile sensor, which is used for sensory neuroprostheses in rats. Unlike most of the previous designs, we used a 3D-printed PLA substrate for lower cost and ease of manufacture. The sensor included a 2×7 array of cells, and each cell consisted of 4 strain gauges connected in series. In order for the sensor to tolerate high displacements in the proposed application, a layer of PDMS was bonded on top of the PI sheet. Two sensors with different PDMS thickness were completed. Static and dynamic characterization of the sensors were also measured.

As mentioned in introduction section, the sensor should have specific features to make it suitable for the purpose of our neuroprostheses application. Now that we fabricated and characterized the sensor, we shall compare the outcomes of the work with our expectations. In following paragraphs, this comparison between the expectations and results will be indicated.

As we mentioned earlier we expect to have a good sensitivity for the fabricated strain gauge array. According to the thickness of the PDMS layer, line-width of the deposited strain gauges, size of the square cells, the sensitivity of the sensor may change. As long as the minimum deformation by the stimulation probes can be detectable using the sensor, its response is acceptable. So, the sensitivity (70-200 mΩ/N) is adequate for neuroprosthetics applications.

We expected to have a sensor with max tolerable force of at least 3N. After characterizing they showed good linearity in the range of 0-4 N and can be used up to 0.9-mm static displacements. We expect that our sensor should not be prone to EMI. However, we could not test the full dynamic range because of EMI in the measurement setups, since the connectors and wires did not have enough isolation to EMI which can be eliminated by better isolation and using specific shielding in foregoing experiments.

Easy, inexpensive, durable and robust fabrication method were among our considerations. To satisfy the mentioned criteria, we used 3D printed substrate instead of Si-

based sensors. We kept the fabrication process simple, inexpensive and time efficient by using transparent film mask for lithography with the minimum line width of 20 μm. The width can be decreased to 2 μm by using more expensive soda-lime glass masks. We also used 3D printer with layer resolution of 100 μm and a positioning precision of 11 μm in the xy-plane. These specifications were adequate for our application. In addition, PLA substrate is biodegradable and embeddable with the boot built for the rats, it also enabled easy bonding with PI which carried the metal strain gauges. However, initially we observed some mechanical stress in the bonded PI-PDMS sample due to thermal expansion mismatch. But after cooling, the PDMS surface was straightened with a glass slide and the PI surface was bonded to PLA substrate under pressure. At the end of this process, we did not observe a detachment of the PDMS or a degradation in the general performance of the sensor. Using this simple, efficient and inexpensive fabrication method, in case of any damages to the array, we could change the damaged sensor with a new one.

Since we did not use a Wheatstone configuration, we do not expect a serious asymmetry problem related to this. It is possible that some offset because of the forces generated by interconnections and alignment. This would affect some strain gages more than others, but since we have 4 strain gages in series for each cell, the interconnect alignment/contact effects would be averaged out.

We needed an array with low cross-talk between the cells. In our fabricated sensor the measured cross talk was less than 5 mΩ/N, which was much less than the sensitivity of the cells. So, in this case the fabricated sensor satisfied our previous expectations also.

Another consideration that we took for designing the sensor was its comparable stiffness to rats' skin stiffness to mimic the tactile feedback originating in the mechanoreceptors of the skin. Specifically, the vibrotactile stimulator system used in the article was designed for applying controlled displacements on the skin surface. Its mechanical impedance is high compared to the skin and allows fast and accurate response with arbitrary waveforms. If the sensor surface is considerably stiff, the stimulator response may be affected. After measuring stiffness of the sensor using graphs presented in figure 5.2 with stiffness of rats' skin, they showed an acceptable result.

The sensor should have linear static and dynamic responses in the deformation range used for the experiments. The frequency response was measured to be flat within 7-15 dB in the range of 2-500 Hz at a given displacement input. Since the vibrotactile stimulation system of the operant chamber is calibrated at every frequency tested in the rat experiments, the deviation from a flat frequency response does not pose a problem, and can be compensated computationally. However, the source of this deviation is not known at this time.

It was shown that PDMS thickness influences the sensitivity of the sensor to a great extent. Tactile neuroprosthetics applications require a relatively thick interface to allow large deformations just like the biological skin. Therefore, it is crucial to optimize all sensor components to achieve the highest sensitivity. In our design, this may be achieved by improving the strain gauge patterning. In order to keep the fabrication costs lower, and to eliminate delays in fabrication process, we used regular cheap mask for lithography. So, the only limitation in shrinking the line width was the accuracy of these masks, which in our case its minimum line width was 20 μm. However, more expensive and more accurate printed mask can shrink this size down to 2 μm. The practical choice for thickness was 50 nm based on our previous experience.

The boot is designed such that it is isolated the rats' mechanoreceptors from stimulation probes of the floor. The tactile neuroprostheses setup has been designed for real-time experiments instead of recording the results and post-processing on them. The main research focuses on microstimulation of the somatosensory cortex in the brain.

7. FUTURE WORK

As mentioned earlier, we used common inexpensive mask for lithography purposes. Using this mask the minimum achieved line-width can not be lower than 20 μm, which limits the sensitivity of the strain gauges. However, the width can be decreased to 2 μm by using more expensive soda-lime glass masks. Therefore, by using a more accurate and expensive mask we can increase the sensitivity of the sensor even further.

The resolution of the PLA layer printed with the desktop 3D printer that we used is around 100 μm, which limits the accuracy of the cavities built for the membrane. With less accurate 3D-printed product, the accuracy of the alignment decreases and consequently the sensitivity of the different arrays may also differ from each other. So that, the calibration results would not be so precise. To address this issue, and to make the final product more precise, we can use a 3D printer with higher resolution and less unevenness on the printed product.

Another change which the sensor can undertake to make it more robust and durable during the calibration and animal experiments is that we can change the regular copper pins with spring-loaded pins. By using these pins, stress and damage on the Al pads will be minimized.

In order to use all the cells of the array for our experiment, we need a multichannel interface. This interface should have an individual current source for each column. Figure 7.1 shows an example of this interface which can be used to send the signals from each group of strain gauges to the input of an ADC. This interface has two columns of strain gauges, each of which has six group of strain gauges in. For each column, a separate constant current is used. The current is controlled by using the Rset resistance in an LM134 constant current IC. In our case we adjust the Rset such that a constant current of 1 mA is obtained. In order to decrease the usage of inputs of ADC channels, we used a decoder which sequentially activates a raw of strain gauges with switching transistors. According to the maximum operation frequency in animal experiments, the clock frequency for controlling the control signals can be determined. Simultaneously, at each clock edge the changes in a raw of strain

gauges, including two vertical strain gauges, are measured and after being amplified and band pass filtering is sent to the inputs of an ADC. Then the digitalized signals are monitored and plotted using a manual software in MATLAB.

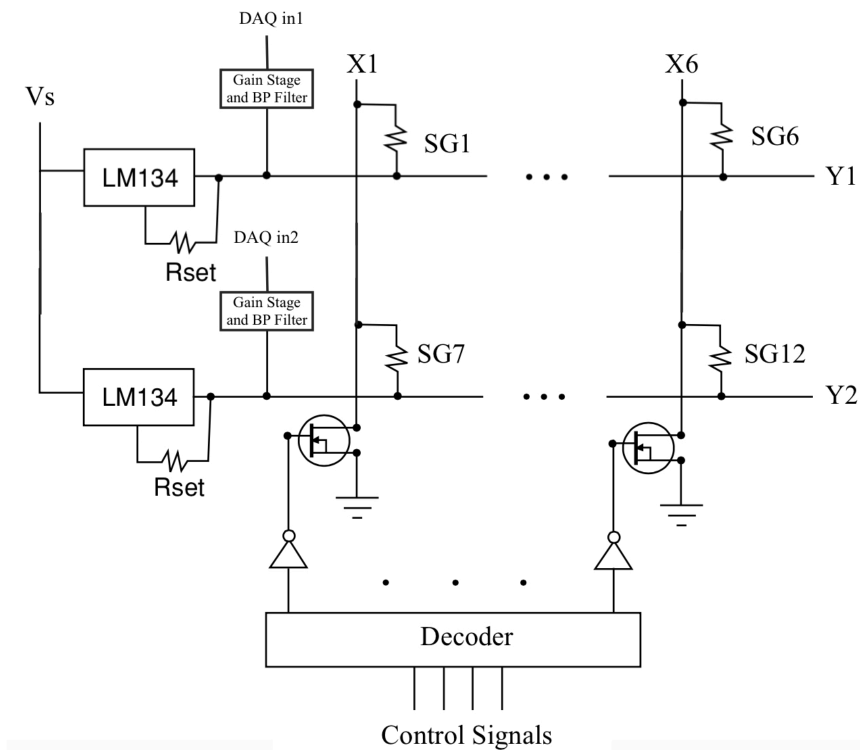

Figure 7.1. The interface which can be used for preparation the sensor signals prior to send to the inputs of an ADC

As mentioned above this strain gauge array can be used for detection of both static and dynamic stimulations. For the purpose of measuring static indentation, a constant current is flown in the strain gauges and voltage changes generated by resistance changes should be amplified and then conveyed to the ADC. To do this process a DC amplifier is needed. Also, initial DC offset caused by the nominal resistance of the strain gauges should be eliminated. We can use a fully-differential stage followed by a gain stage to eliminate the offset and amplify the DC signals.

Integration of the sensor with the boot designed for hind paws of rats for neuroprosthesis experiments on rats is another future plan. Using plastic clips designed on the boot or liquid adhesive, the boot can hold the sensor firmly. Moreover, we used Omnetics micro-connector to make the integration even simpler. Litz wire will be used for connecting the sensor to the electronics circuit to give more freedom to the rat while performing the neuroprosthesis experiments inside the conditioning chamber. A flexible aluminum shield will cover the litz wire to minimize 50 cycle noise caused by resources placed outside of the chamber as well as the mechanical shaker inside the chamber.

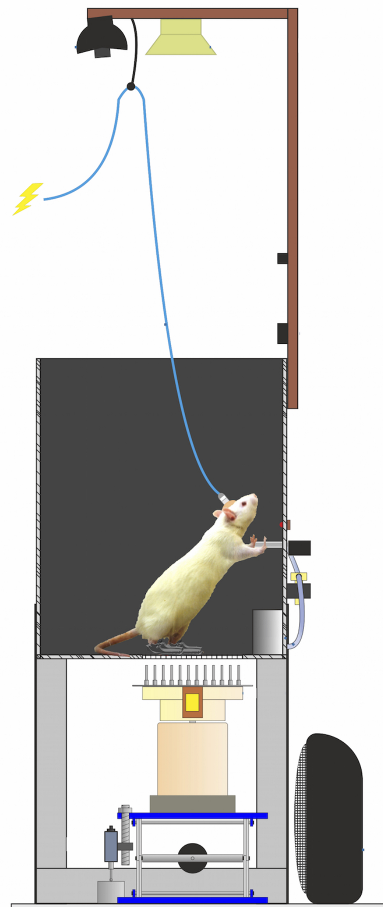

Figure 7.2. An illustration of the conditioning chamber, mechanical stimulation system, and a rat with implanted electrodes in its somatosensory cortex, performing tactile neuroprosthesis experiment [64].

Even more flexibility and freedom can be provided in the experiments by using miniature wireless transceiver modules. We can place the module inside the boot or a small bag fastened to the back of a rat. All the electronics circuits and interfaces can be integrated and shrunk such that they can be placed inside the rat's bag. The outputs of the receiver are connected to the ADC and then detected signals are measured using this approach.

The multichannel feature of the tactile sensor was not utilized in the application presented here, because of the simplicity of the experimental paradigm used in rats. However, a similar design may be used in the future to cover prosthetic fingers for monkeys and humans. In that case, distributed sensing can help for object recognition and texture perception. Spatiotemporal activation of individual channels of the tactile sensor would give much more information than that obtained in the point-wise temporal stimulation discussed in this work.

And finally we will use the sensor with integrated boot to emulate the operation of tactile neuroprosthesis in behaving rats, as illustrated in figure 1 and was explained in section 1. Figure 7.2 shows the conditioning chamber and a rat performing tactile neuroprosthesis experiment [64].

REFERENCES

1. Green, A., C. Chapman, J. Kalaska and F. Lepore, "Sensory feedback for upper limb prostheses", *Enhancing Performance for Action and Perception: Multisensory Integration, Neuroplasticity and Neuroprosthetics*, p. 69, 2011.

2. Weber, D. J., R. Friesen and L. E. Miller, "Interfacing the Somatosensory System to Restore Touch and Proprioception: Essential Considerations", *Journal of Motor Behavior*, Vol. 44, No. 6, pp. 403-418, 2012.

3. Bensmaia, S. J. and L. E. Miller, "Restoring sensorimotor function through intracortical interfaces: progress and looming challenges", *Nature reviews Neuroscience*, Vol. 15, No. 5, pp. 313-325, 2014.

4. Berg, J. A., J. F. D. III, F. V. Tenore, G. A. Tabot, J. L. Boback, L. R. Manfredi, M. L. Peterson, K. D. Katyal, M. S. Johannes, A. Makhlin, R. Wilcox, R. K. Franklin, R. J. Vogelstein, N. G. Hatsopoulos and S. J. Bensmaia, "Behavioral Demonstration of a Somatosensory Neuroprosthesis", *IEEE Transactions on Neural Systems and Rehabilitation Engineering,* Vol. 21, No. 3, pp. 500-507, 2013.

5. Tabot, G. A., J. F. Dammann, J. A. Berg, F. V. Tenore, J. L. Boback, R. J. Vogelstein and S. J. Bensmaia, "Restoring the sense of touch with a prosthetic hand through a brain interface", *Proceedings of the National Academy of Sciences*, Vol. 110, No. 45, pp.18279-18284, 2013.

6. Horch, K., S. Meek, T. G. Taylor and D. T. Hutchinson, "Object Discrimination with an Artificial Hand Using Electrical Stimulation of Peripheral Tactile and Proprioceptive Pathways with Intrafascicular Electrodes", *IEEE Transactions on Neural Systems and Rehabilitation Engineering*, Vol. 19, No. 5, pp. 483-489, 2011.

7. Raspopovic, S., M. Capogrosso, F. M. Petrini, M. Bonizzato, J. Rigosa, G. Di Pino, J. Carpaneto, M. Controzzi, T. Boretius, E. Fernandez, G. Granata, C. M. Oddo, L. Citi,

A. L. Ciancio, C. Cipriani, M. C. Carrozza, W. Jensen, E. Guglielmelli, T. Stieglitz, P. M. Rossini and S. Micera, “Restoring Natural Sensory Feedback in Real-Time Bidirectional Hand Prostheses”, *Science Translational Medicine*, Vol. 6, No. 222, pp. 222ra19-222ra19, 2014.

8. Devecioğlu, İ. and B. Güçlü, “A novel vibrotactile system for stimulating the glabrous skin of awake freely behaving rats during operant conditioning”, *Journal of Neuroscience Methods*, Vol. 242, pp. 41-51, 2015.

9. Lee, K. R., K. Kim, Y. K. Kim, D. S. Lee, W. H. Kim, N. K. Cho, K. B. Park, K. S. Shin and H. D. Park, “Fabrication of Polymer-based Flexible Tactile Sensing Module with Metal Strain Gauges and Interconnecter”, *Sensors, 2006. 5th IEEE Conference on*, pp. 742-745, 2006.

10. Lee, H. K., J. Chung, S. I. Chang and E. Yoon, “Normal and Shear Force Measurement Using a Flexible Polymer Tactile Sensor with Embedded Multiple Capacitors”, *Journal of Microelectromechanical Systems*, Vol. 17, No. 4, pp. 934-942, 2008.

11. Muhammad, H., C. Oddo, L. Beccai, C. Recchiuto, C. Anthony, M. Adams, M. Carrozza, D. Hukins and M. Ward, “Development of a bioinspired MEMS based capacitive tactile sensor for a robotic finger”, *Sensors and Actuators A: Physical*, Vol. 165, No. 2, pp. 221-229, 2011.

12. Wen, C.-C. and W. Fang, “Tuning the sensing range and sensitivity of three axes tactile sensors using the polymer composite membrane”, *Sensors and Actuators A: Physical*, Vol. 145-146, pp. 14-22, 2008.

13. Hu, C. F., H. Y. Huang, C. C. Wen, L. Y. Lin and W. Fang, “Implementation of a flexible silicon-based tactile sensor array”, *Sensors, 2010 IEEE*, pp. 1736-1739, 2010.

14. Kon, S. and R. Horowitz, “A High-Resolution MEMS Piezoelectric Strain Sensor for Structural Vibration Detection”, *IEEE Sensors Journal*, Vol. 8, No. 12, pp. 2027-2035, 2008.

15. Kim, M. S., H. R. Ahn, S. Lee, C. Kim and Y. J. Kim, “A dome-shaped piezoelectric tactile sensor arrays fabricated by an air inflation technique”, *Sensors and Actuators A: Physical*, Vol. 212, pp. 151-158, 2014.

16. Zhang, Y., “Sensitivity enhancement of a micro-scale biomimetic tactile sensor with epidermal ridges”, *Journal of Micromechanics and Microengineering*, Vol. 20, No. 8, p. 085012, 2010.

17. Hwang, E. S., J. h. Seo and Y. J. Kim, “A Polymer-Based Flexible Tactile Sensor for Both Normal and Shear Load Detections and Its Application for Robotics”, *Journal of Microelectromechanical Systems*, Vol. 16, No. 3, pp. 556-563, 2007.

18. Engel, J., J. Chen and C. Liu, “Development of polyimide flexible tactile sensor skin”, *Journal of Micromechanics and Microengineering*, Vol. 13, No. 3, p. 359, 2003.

19. Timoshenko, S. and J. Goodier, *Theory of elasticity*, McGraw-Hill book Company, New York, USA, 1951.

20. Senturia, S. D., *Microsystem design*, Kluwer Academic Publishers, New York, USA, 2002.

21. Bao, M., *Analysis and design principles of MEMS devices*, Elsevier Inc., San Diego, CA, USA, 2005.

22. Kumar, N., *Comprehensive physics XII*, Laxmi Publications, Daryaganji, New Delhi, India, 2003.

23. Mark, J. E., H. R. Allcock and R. West, *Inorganic polymers*, Oxford University Press, New York, USA, 2005.

24. Noll, W., *Chemistry and technology of silicones*, ACADEMIC PRESS Inc., Leverkuen, Germany, 2012.

25. Meals, R., "Kirk-Othmer encyclopedia of chemical technology", Wiley-Interscience, New York, 1969.

26. Borisov, S. N., *Organosilicon heteropolymers and heterocompounds*, Springer Science & Business Media, New York, USA, 2012.

27. Morton, M., *Rubber Technology*, Van Nostrand Reinhold Co., New York, USA, 1987.

28. Mark, J. E., D. W. Schaefer and G. Lin, *The polysiloxanes*, Oxford University Press, Madison Avenue, New York, USA, 2015.

29. Allcock, H. R., *Scientific American*, Nature America, Inc., Vol. 230, No. 3, p. 66., 1974

30. Allcock, H. R., "Heteroatom ring systems and polymers", NY: Academic, USA, 1967.

31. Elias, H.-G., *Macromolecules: Volume 2: Synthesis, Materials, and Technology*, Springer, 2013.

32. Noshay, A. and J. E. McGrath, *Block copolymers: overview and critical survey*, Elsevier, 2013.

33. Mark, J. E., *Macromulecules*, ACS Publications, Vol. 11, p. 627, 1978.

34. Warrick, E., O. Pierce, K. Polmanteer and J. Saam, "Rubber Chem*", Tech*, Vol. 52, No. 3, p. 437, 1979.

35. Ghodssi, R. and P. Lin, *MEMS materials and processes handbook*, Vol. 1, Springer Science & Business Media, College Park, Maryland, USA, 2011.

36. Chakravartula, A. and K. Komvopoulos, "Viscoelastic properties of polymer surfaces investigated by nanoscale dynamic mechanical analysis", *Applied Physics Letters*, Vol. 88, No. 13, 2006.

37. Ginn, B. T., and O. Steinbock, “Polymer Surface Modification Using Microwave-Oven-Generated Plasma”, *Langmuir*, Vol. 19, No. 19, pp. 8117-8118, 2003.

38. Hillborg, H., J. Ankner, U. Gedde, G. Smith, H. Yasuda and K. Wikstrom, “Crosslinked polydimethylsiloxane exposed to oxy- gen plasma studied by neutron reflectometry and other surface specific techniques”, *Polymer*, Vol. 41, No. 18, pp. 6851-6863, 2000.

39. Li, X., N. Wu, Y. Rojanasakul and Y. Liu, “Selective stamp bonding of PDMS microfluidic devices to polymer substrates for biological applications”, *Sensors and Actuators A: Physical*, Vol. 193, pp. 186-192, 2013.

40. Sasaki, S., T. Kon and T. Ohsaki, “A new multi-chip module using a copper polyimide multi-layer substrate”, *Electronic Components Conference*, *1989. Proceedings., 39th,* pp. 629–635, May 1989.

41. Ordonez, J. S., C. Boehler, M. Schuettler and T. Stieglitz, “Silicone rubber and thin-film polyimide for hybrid neural interfaces; A MEMS-based adhesion promotion technique”, *Neural Engineering (NER), 2013 6th International IEEE/EMBS Conference on*, pp. 872–875, Nov 2013.

42. Hotta, Y., Y. Zhang and N. Miki, “A Flexible Capacitive Sensor with encapsulated Liquids as Dielectrics”, *Micromachines*, Vol. 3, No. 1, p. 137, 2012.

43. Pizzi, A. and K. L. Mittal, *Handbook of adhesive technology, revised and expanded*, Macel Deker, Madison Avenue, New York, NY, USA, 2003.

44. Boenig, H. V., *Plasma science and technology*, Cornell University Press, New York, USA, 1982.

45. Rantz, E., *Adhesive Age*, Chemical Week Associates, New York, USA, May 1978.

46. Prane, W., *Adhesive age*, Chemical Week Associates, New York, USA, June 1989.

47. Petrie, E. M., *Adhesive Age*, Chemical Week Associates, New York, USA, May 1989.

48. Plummer, J. D., *Silicon VLSI technology: fundamentals, practice, and modeling*, Prentice Hall, Inc., Upper Saddle River, New Jersey, USA, 2009.

49. Application notes, MicroChemicals GmbH, Ulm, Germany, “Aluminum Etching”, 2013, www.microchemicals.com/downloads/application_notes.html, accessed at June 2016.

50. Bao, M., *Analysis and design principles of MEMS devices*, Elsevier Inc., San Diego, CA, USA, 2005.

51. Timoshenko, S. P. and S. Woinowsky-Krieger, *Theory of plates and shells*, McGraw-hill, New York, USA, 1959.

52. Dargahi, J., “A piezoelectric tactile sensor with three sensing elements for robotic, endoscopic and prosthetic applications”, *Sensors and Actuators A: Physical*, Vol. 80, No. 1, pp. 23-30, 2000.

53. Yousef, H., M. Boukallel and K. Althoefer, “Tactile sensing for dexterous in-hand manipulation in robotics: A review”, *Sensors and Actuators A: Physical*, Vol. 167, No. 2, pp. 171-187, 2011.

54. Li, X., N. Wu, Y. Rojanasakul and Y. Liu, “Selective stamp bonding of PDMS microfluidic devices to polymer substrates for biological applications”, *Sensors and Actuators A: Physical*, Vol. 193, pp. 186-192, 2013.

55. Hotta, Y., Y. Zhang and N. Miki, “A Flexible Capacitive Sensor with Encapsulated Liquids as Dielectrics”, *Micromachines*, Vol. 3, No. 1, p. 137, 2012.

56. Ordonez, J. S., C. Boehler, M. Schuettler and T. Stieglitz, “Silicone rubber and thin-film polyimide for hybrid neural interfaces; A MEMS-based adhesion promotion technique”, *Neural Engineering (NER), 2013 6th International IEEE/EMBS Conference on*, pp. 872-875, Nov 2013.

57. Güçlü, B. and C. Oztek, “Tactile sensitivity of children: Effects of frequency, masking, and the non-Pacinian I psychophysical channel”, *Journal of Experimental Child Psychology*, Vol. 98, No. 2, pp. 113-130, 2007.

58. Güçlü, B., “Deviation from Weber’s law in the non-Pacinian I tactile channel: A psychophysical and simulation study of intensity discrimination”, *Neural computation*, Vol. 19, No. 10, pp. 2638-2664, 2007.

59. Yildiz, M. Z. and B. Güçlü, “Relationship between vibrotactile detection thresh- old in the Pacinian channel and complex mechanical modulus of the human glabrous skin”, *Somatosensory & Motor Research*, Vol. 30, No. 1, pp. 37-47, 2013.

60. Güçlü, B. and S. J. Bolanowski, “Frequency responses of cat rapidly adapting mechanoreceptive fibers”, *Somatosensory & Motor Research*, Vol. 20, No. 3-4, pp. 249-263, 2003.

61. Devecioglu, I. and B. Güçlü, “Asymmetric response properties of rapidly adapting mechanoreceptive fibers in the rat glabrous skin”, *Somatosensory & Motor Research*, Vol. 30, No. 1, pp. 16-29, 2013.

62. Güçlü, B., “Low-cost computer-controlled current stimulator for the student lab- oratory”, *Advances in Physiology Education*, Vol. 31, No. 2, pp. 223-231, 2007.

63. Kuyumcu, F., O. Erdogan and B. Güçlü, “Electrical nerve stimulation method for intraoperative localization of the inferior alveolar nerve within the mandible: a pilot study in rabbits”, *International Journal of Oral and Maxillofacial Surgery*, Vol. 44, No. 11, pp. 1398-1404, 2015.

64. Devecioğlu İ, Güçlü B, “Electrical microstimulation of hindpaw representation in rat SI cortex yeilds better detection probibility compared to vibrotactile stimulation of the glaborous skin during operant conditioning.”, Program No. 64.12. 2014 Neuroscience Meeting Planner. Washington, DC: *Society for Neuroscience*, 2014.

65. Beygi, M., Mutlu, S., and Güçlü, B., “Microfabricated strain gauge array on polymer substrate for tactile neuroprostheses in rats”, *Journal of Micromechanics and Microengineering,* In press.

APPENDIX A: SENSOR MASK

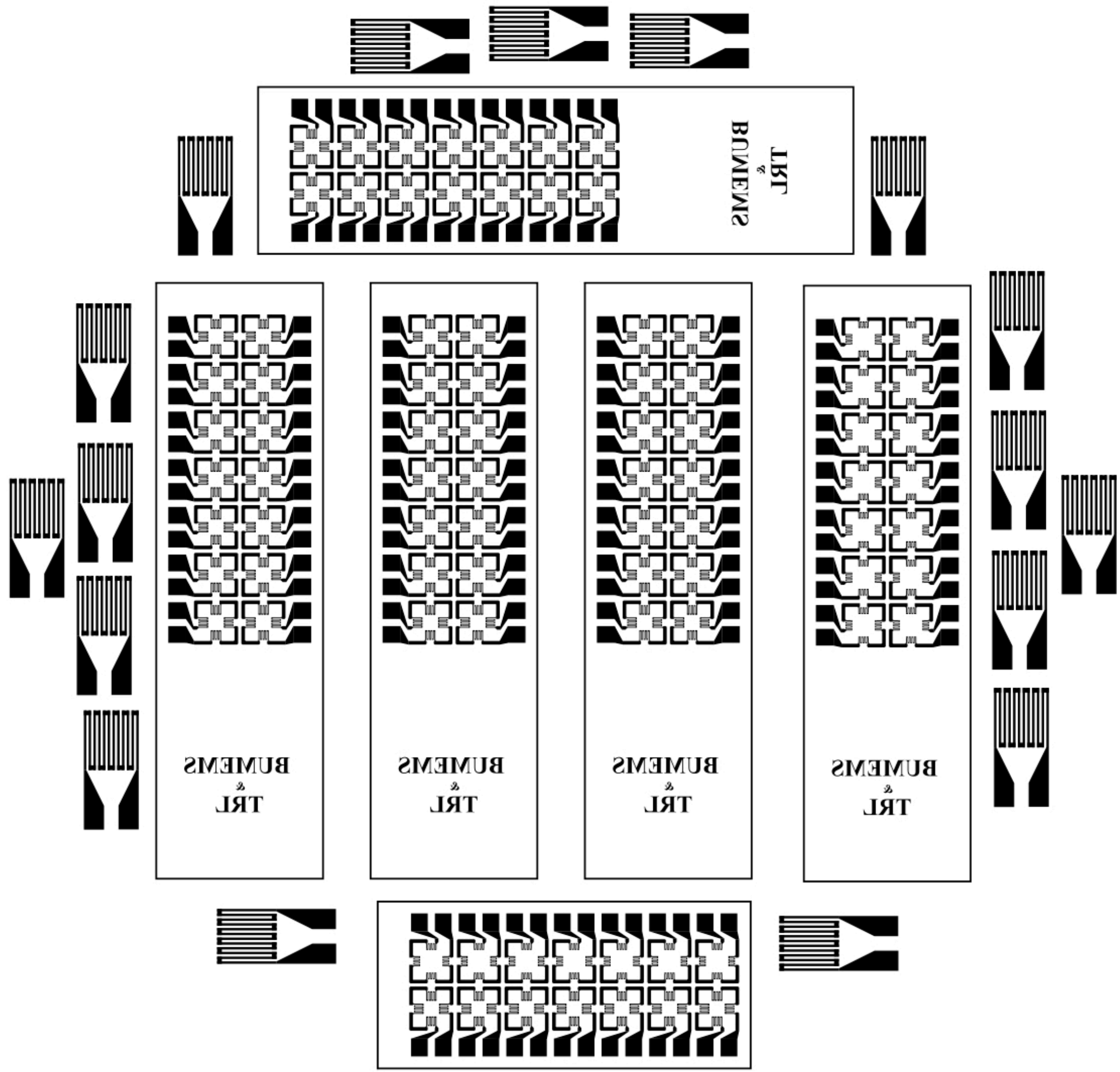

Figure A.1. Lithography mask.

APPENDIX B: SAMPLES OF RECORDED RESULTS

B.1. Samples of Static Results

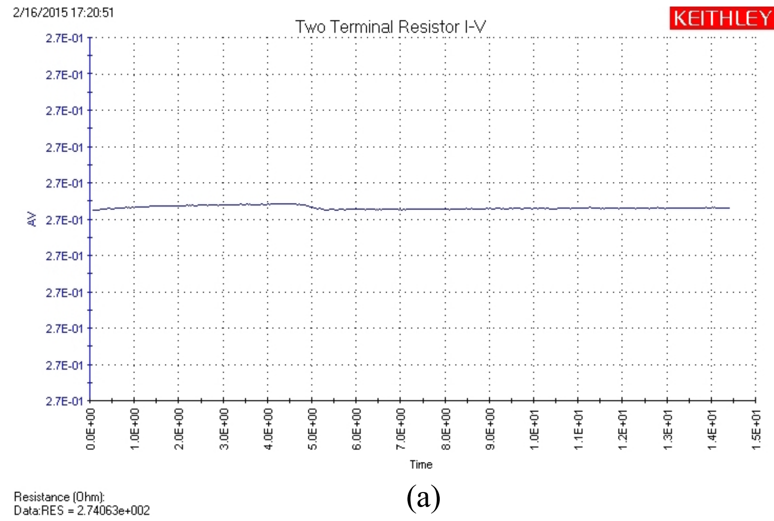

(a)

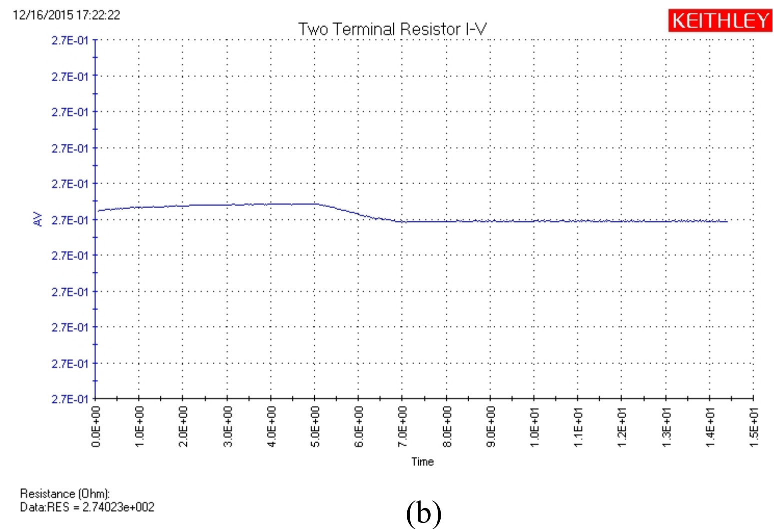

(b)

Figure B.1. Voltage variation results obtained by DC characterization system while various forces were applied on top of a square membrane.

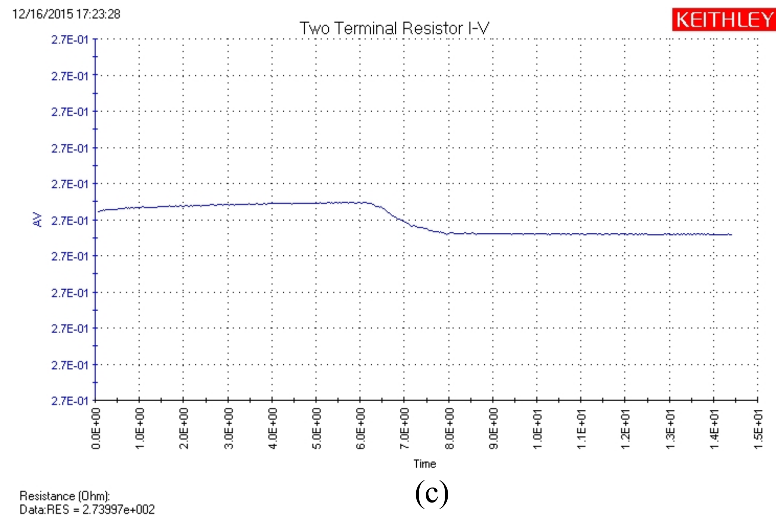

(c)

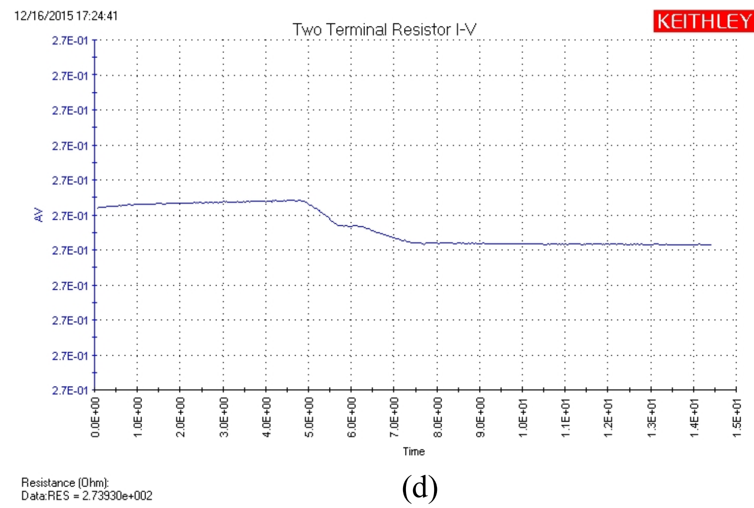

(d)

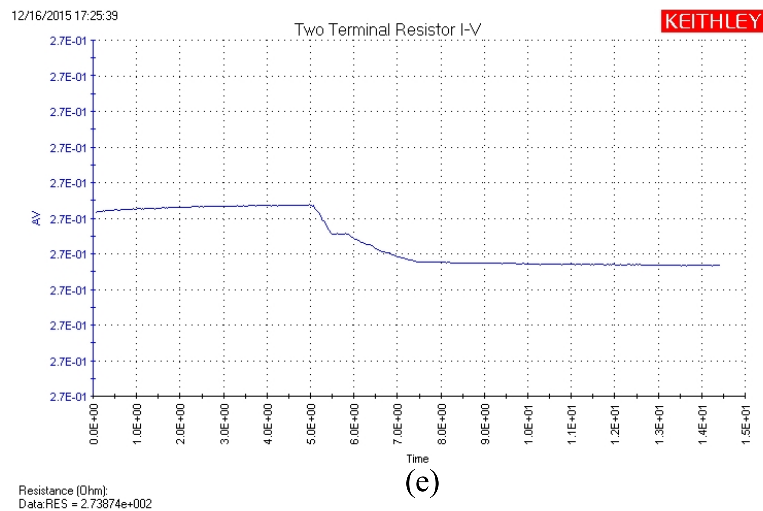

(e)

Figure B.1. Voltage variation results obtained by DC characterization system while various forces were applied on top of a square membrane. (cont.)

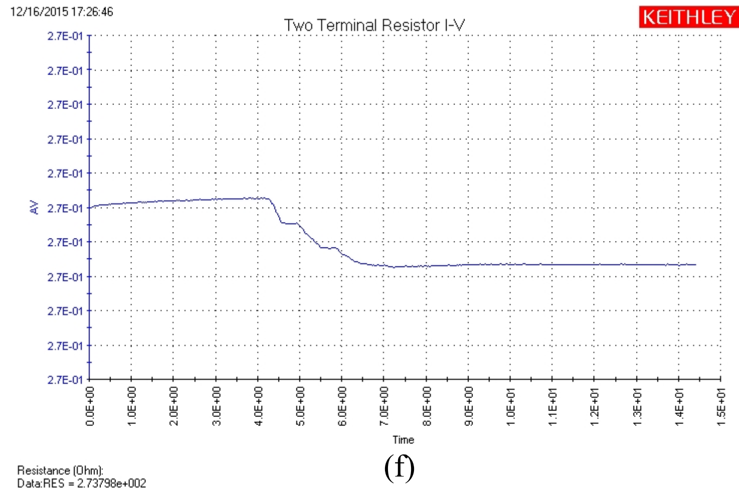

(f)

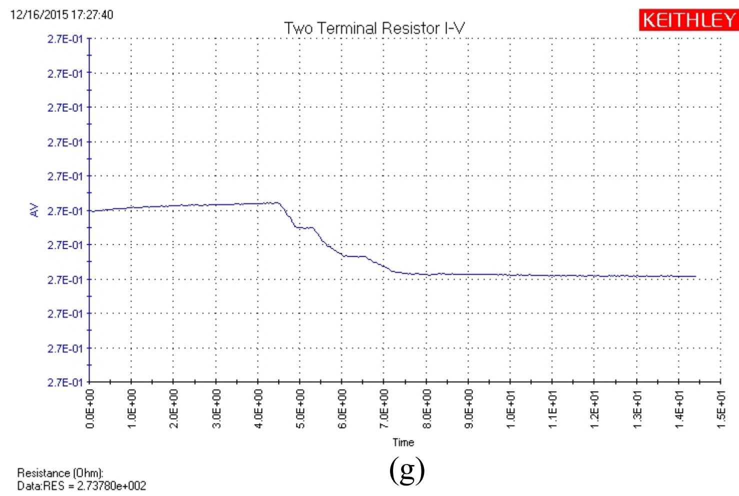

(g)

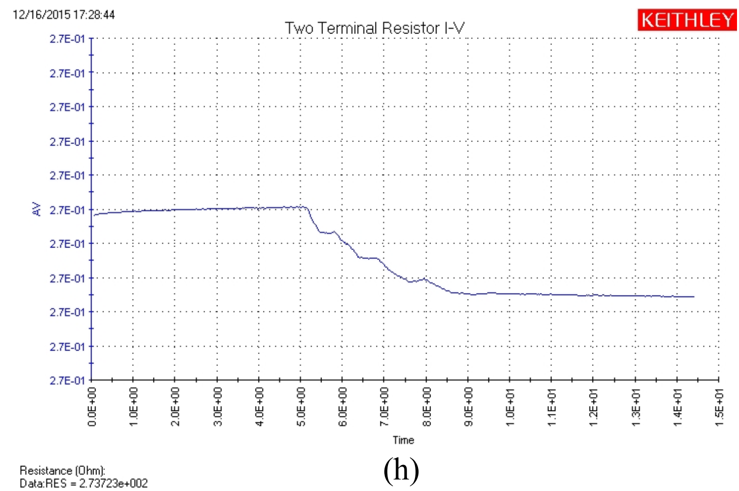

(h)

Figure B.1. Voltage variation results obtained by DC characterization system while various forces were applied on top of a square membrane. (cont.)

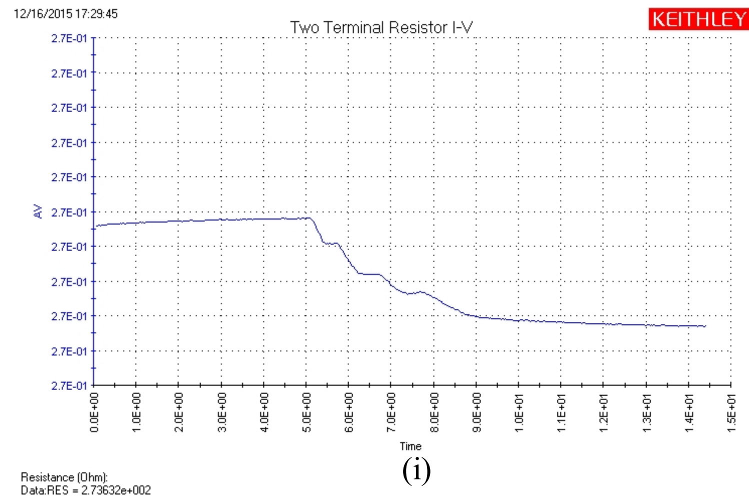

(i)

Figure B.1. Voltage variation results obtained by DC characterization system while various forces were applied on top of a square membrane. (cont.)

B.2. A Sample of Dynamic Results

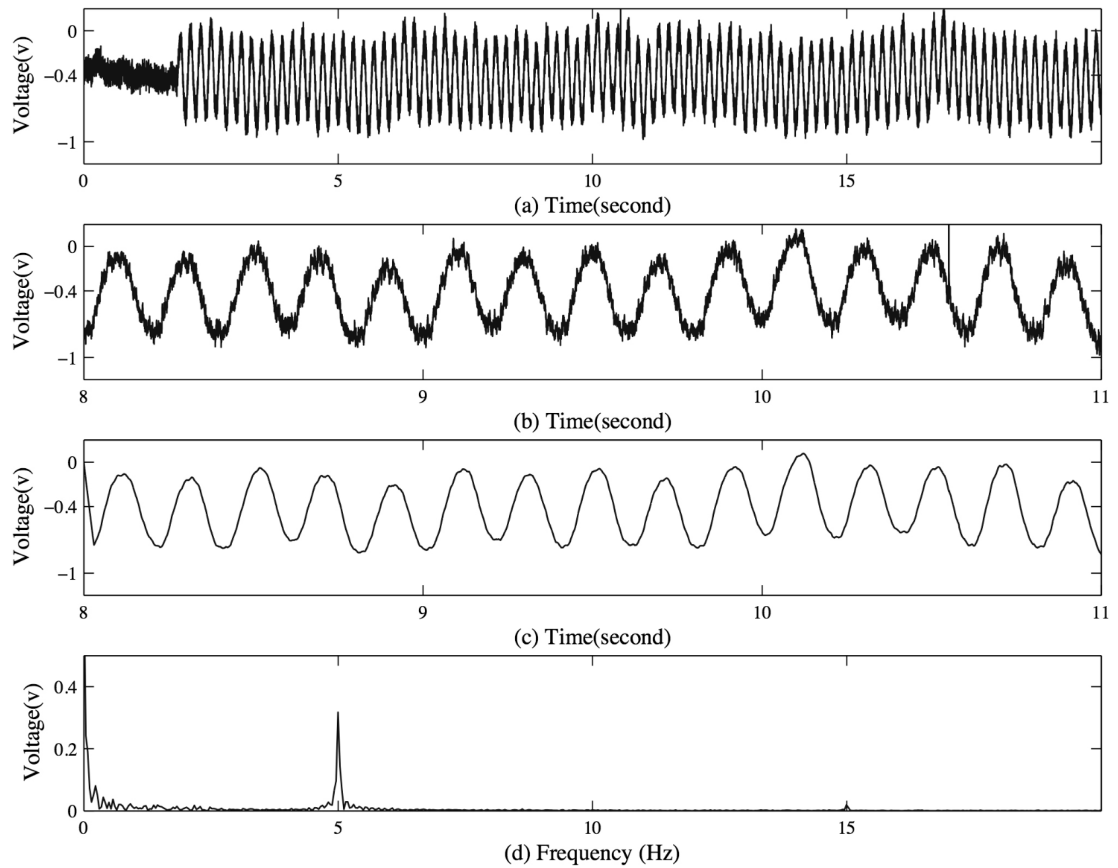

Figure B.2. Dynamic signal recorded from sensor, when the mechanical shaker stimulated a membrane with the frequency of 5 Hz. (a) dynamic signal recorded after 10 k voltage amplification (b) 3 seconds of recorded signal (c) a portion of the recorded signal after off-line high frequency filtering (d) FFT of the signal shown in (a), y-axis shows peak-to-peak of the sinusoidal signal in (a).